



저작자표시-비영리-변경금지 2.0 대한민국

이용자는 아래의 조건을 따르는 경우에 한하여 자유롭게

- 이 저작물을 복제, 배포, 전송, 전시, 공연 및 방송할 수 있습니다.

다음과 같은 조건을 따라야 합니다:



저작자표시. 귀하는 원저작자를 표시하여야 합니다.



비영리. 귀하는 이 저작물을 영리 목적으로 이용할 수 없습니다.



변경금지. 귀하는 이 저작물을 개작, 변형 또는 가공할 수 없습니다.

- 귀하는, 이 저작물의 재이용이나 배포의 경우, 이 저작물에 적용된 이용허락조건을 명확하게 나타내어야 합니다.
- 저작권자로부터 별도의 허가를 받으면 이러한 조건들은 적용되지 않습니다.

저작권법에 따른 이용자의 권리는 위의 내용에 의하여 영향을 받지 않습니다.

이것은 [이용허락규약\(Legal Code\)](#)을 이해하기 쉽게 요약한 것입니다.

[Disclaimer](#)

공학박사 학위논문

**Charge Generation of
n-doped Organic Semiconductors
and Polaron Transport in
Organic Light-Emitting Diodes
for Operational Stability**

n-도핑된 유기반도체의 전하생성효율과
유기발광소자의 구동 안정성을 위한
폴라론 거동 분석

2018년 8월

서울대학교 대학원
하이브리드재료 전공
김재민

**Charge Generation of
n-doped Organic Semiconductors
and Polaron Transport in
Organic Light-Emitting Diodes
for Operational Stability**

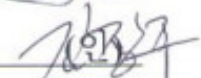
지도 교수 김 장 주

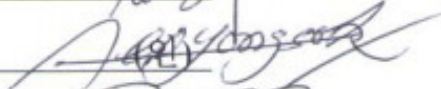
이 논문을 공학박사 학위논문으로 제출함
2018년 8월

서울대학교 대학원
하이브리드재료 전공
김 재 민

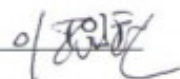
김재민의 공학박사 학위논문을 인준함
2018년 8월

위 원 장 _____ 윤 재 루 (인) 

부위원장 _____ 김 장 주 (인) 

위 원 _____ 서 용 석 (인) 

위 원 _____ 홍 종 인 (인) 

위 원 _____ 이 재 현 (인) 

Abstract

**Charge Generation of
n-doped Organic Semiconductors
and Polaron Transport in
Organic Light-Emitting Diodes
for Operational Stability**

Jae-Min Kim

Department of Materials Science and Engineering

The Graduate School

Seoul National University

Discovery of organic semiconductors enables a variety of organic electronic devices involving organic light-emitting diodes (OLEDs), organic photovoltaics, organic thin-film transistors. Especially, OLEDs has been commercialized and became practical display based on the establishment of chemical and physical understanding of organic semiconductors. In this research, charge in electrically doped organic semiconductors and OLEDs is

explored. First, charge generation mechanism of *n*-type-doped organic semiconductors is investigated. Second, operational stability of OLEDs is correlated with polaron behaviors in view of polaron and exciton distribution. In chapter 2, charge generation process in electrically doped organic semiconductors is quantitatively analyzed. Electrical doping is an important technology to enhance the conductivity of organic layers, which is related to driving voltage and corresponding efficiency of organic electronic devices. In organic semiconductors, the charge generation efficiency, the ratio between generated charge carriers and dopants, shows a few percents, which is a different behavior to conventional inorganic semiconductors. Many reports revealed that doping effect is realized by the formation of charge transfer complex and dissociation into free charge carrier. In this research, for *n*-type doped organic semiconductors, the charge transfer complex formation efficiency and dissociation efficiency depending on dopant concentration are quantitatively analyzed. As a result, it is investigated that dissociation into free charge carrier is relatively inefficient compared to formation of charge transfer complex.

In chapter 3 and 4, electrical properties of materials and device are correlated with the operational stability of OLEDs. In chapter 3, from a comparison of the co-host based device and single host based device, it is verified that polaron and exciton distribution under the operation is dependent on the balance between electron and hole mobilities. This finding means that quantitative characterization of mobility balance in the EML is crucial to enhance device

stability of OLEDs in addition to the use of co-host or bipolar host. In chapter 4, the role of charge transport layer in device stability of OLEDs is revealed. With the modification of HTLs only in the device structure, device lifetime is seven-times enhanced in comparison of two kinds of OLEDs. From various static and dynamic electrical characterization of materials and devices, it is unraveled that charge transport layers control the number of charge carriers in the EML and induces charge transport path in the EML. These two effects are important in carrier balance in the EML in terms of carrier density balance and carrier mobility balance, which affects exciton and polaron density distribution. Therefore, it implies that electrical consideration of charge transport layers should be performed in comprehensive views in order to enhance operational stability of OLEDs.

Keywords: organic semiconductors, organic light-emitting diodes, electrical doping, device stability, polaron behavior, impedance spectroscopy, drift-diffusion modeling

Student Number: 2012 - 23928

Abstract	i
Contents	iv
List of Tables	viii
List of Figures	ix
Chapter 1. Introduction	1
1.1 Electrical doping in organic semiconductors	1
1.2 Operational stability of organic light-emitting diodes	8
1.3 Theoretical description of electrical characteristics of OLEDs (Drift-diffusion numerical modeling).....	15
1.4 Impedance spectroscopy	21
Chapter 2. N-Type Molecular Doping in Organic Semiconductors: Formation and Dissociation Efficiencies of a Charge Transfer Complex	36
2.1 Introduction.....	36
2.2 Experimental methods	39
2.3 Charge transfer complex formation efficiency	40

2.4 Decomposition of Rb_2CO_3 based on in situ XPS measurements.	46
2.5 Charge generation efficiency and dissociation efficiency.....	49
2.6 Conclusion.	55

Chapter 3. Mobility Balance in the Light-emitting Layer Governs the Polaron Accumulation and Operational Stability of Organic Light-Emitting Diodes.....	57
3.1 Introduction.....	57
3.2 Experimental methods	59
3.3 Structure design and performance of OLEDs.....	59
3.4 Understanding of charge behavior by impedance spectroscopy and drift-diffusion numerical modeling.....	63
3.5 Recombination zone depending on the mobility ratio	71
3.6 Conclusion	73

Chapter 4. Charge Transport Layers Manage Mobility and Carrier Density Balance in Light-emitting Layers Influencing the Operational Stability of Organic Light-emitting Diodes	75
4.1 Introduction.....	75
4.2 Experimental methods	77
4.3 Device structure and performance of OLEDs.....	79
4.4 Charge transport in single carrier devices.....	83
4.5 Impedance analysis of the OLEDs.....	88
4.6 Correlation between the charge transport and operational stability of the OLEDs	92
4.7 Conclusion	95
Chapter 5. Summary and Conclusion	97
Bibliography	101
초록	113
CURRICULUM VITAE	115

List of Publications	117
List of Presentations	118
List of Patents	121
Acknowledgements (감사의 글)	122

List of Tables

Table 3.1 Calculated bond dissociation energies (BDEs, units of eV) of materials used as charge transports and hosts in OLEDs	62
Table 3.2 Physical parameters used in the drift-diffusion numerical simulations.	69
Table 4.1 Performances and lifetimes of devices 1 and 2.....	82

List of Figures

Figure 1.1 Schematic illustration of fundamental processes and main factors of electrical doping in organic semiconductors.....	2
Figure 1.2 Schematic diagram of charge generation mechanisms in electrically doped organic semiconductors.	5
Figure 1.3 Commercial products adopting organic light-emitting diodes. (a) Samsung Galaxy S8 (b) Apple iPhone X (C) LG Signature TV.....	9
Figure 1.4 Schematic diagram of charge generation mechanisms in electrically doped organic semiconductors.....	10
Figure 1.5 History of device lifetime of fluorescent and phosphorescent OLEDs. ^[26]	12
Figure 1.6 Internal and external degradation origins of organic light-emitting diodes	14
Figure 1.7 Schematic diagram of dielectric loss mechanism of materials depending on frequency in view of complex dielectric permittivity.....	23
Figure 1.8 (a) Device structure of metal-insulator-semiconductor (MIS) devices (b) Mott-Schottky plot ($1/C_2-V$) of MIS devices (c) capacitance loss spectrum.	26
Figure 1.9 (a) Negative differential susceptance ($-\Delta B$) spectrum and (b) imaginary Z spectrum of a single carrier device for various DC voltages.	28
Figure 1.10 Schematic description of mechanisms contributing the capacitance of OLEDs.	30

Figure 1.11 Schematic description of principle of charge accumulation and trap-detrap response induced capacitance-frequency spectrums.....32

Figure 2.1 (a) UV-Vis-NIR absorption spectra of Rb₂CO₃-doped TPBi thin film, and (b) calibrated absorption spectra without reflection. The number of TPBi molecules in all sample is fixed as that of the 50 nm TPBi pristine thin film.....42

Figure 2.2 CTC formation efficiency of Rb₂CO₃-doped TPBi thin film with various dopant densities. Dashed line is the linear fit of the data. CTC formation efficiency is the ratio of the number density of CTCs to dopant molecules. The linear decrease of CTC formation efficiency means that both the number and the size of aggregates increase simultaneously.44

Figure 2.3 (In situ) XPS core level spectra of (a) Rb 3d (b) O 1s and (c) C 1s for evaporated Rb₂CO₃ film on Au substrate. The decomposed peaks represent the results of peak fitting with Voigt functions.47

Figure 2.4 (a) Capacitance-voltage characteristics of MIS (metal-insulator-semiconductor) devices at various doping concentrations. (b) Capacitance loss spectrum (G/ω) of MIS devices.51

Figure 2.5 Charge carrier density of Rb₂CO₃-doped TPBi layer from Mott-Schottky analysis. The device structure is ITO (150 nm)/LiF (150 nm)/Rb₂CO₃-doped TPBi (200 nm)/Rb₂CO₃ (1 nm)/Al (100 nm). Dashed line is the linear fit of the data ($N_{free-carrier} = sN_{dopant} + n_0$).52

Figure 2.6 (a) Formation and dissociation efficiencies of CTC. Dotted data are obtained from the experiment. Dashed line is the fitted line of CTC formation

efficiency and the solid lines represent the calculated dissociation efficiency and charge generation efficiency using the constant derived from experimental data. (b) Energetic position of Fermi level relative to donor level based on Fermi-Dirac distribution of single donor level.....54

Figure 3.1 (a) Emitting layer (EML) structures, (b) current density–voltage–luminance (J–V–L) results, (c) external quantum efficiency–luminance (EQE–L) data, and (d) operational lifetimes of exciplex-forming host and single host-based OLEDs. Device lifetimes were measured under the constant current condition at the initial luminance of 1,000 cd m⁻².60

Figure 3.2 (a) Parallel capacitance–voltage characteristics of OLEDs as a function of luminance and current density. The dotted lines are experimental results and the dashed lines are calculated results from drift-diffusion numerical modeling. The frequency and amplitude of the AC voltage were 500 Hz and 100 mV, respectively. (b) Field-dependent electron and hole mobilities of the EMLs. The mobility was obtained by analyzing the space-charge limited current of charge-only devices. (c, d) The distribution of the local charge densities of electrons and holes at different voltages in (c) exciplex-forming and (d) single host-based OLEDs calculated by drift-diffusion simulations.64

Figure 3.3 (a) Current density–voltage characteristics of single carrier devices consisting of an exciplex-forming co-host based emitting layer (EML) and a single host-based EML. (b) Experimental and fitted results of electron and hole mobilities under the application of space-charge limited current. The device structures of the hole- and electron-only devices were indium tin oxide (ITO;

70 nm)/ReO3 (1 nm)/EML (100 nm)/ReO3 (1 nm)/Al (100 nm) and ITO (70 nm)/Rb2CO3 (1 nm)/EML (100nm)/Rb2CO3 (1 nm)/Al (100 nm), respectively.

.....66

Figure 3.4 (a) Calculated local distributions of the exciton generation rates in the EMLs of exciplex-forming co-host- and single host-based OLEDs at 4 V.

(b) Drift-diffusion simulation results of the exciton generation rates assuming different EML mobility ratios. The hole and electron mobilities of each mobility ratio were as follows:

$\mu_{hole} = 2 \times 10^{-8} \text{ cm}^2 \text{ V}^{-1} \text{ s}^{-1}$ and $\mu_{electron} = 2 \times 10^{-8} \text{ cm}^2 \text{ V}^{-1} \text{ s}^{-1}$ ($\gamma_{mobility} = 1$),

$\mu_{hole} = 2 \times 10^{-7} \text{ cm}^2 \text{ V}^{-1} \text{ s}^{-1}$ and $\mu_{electron} = 2 \times 10^{-8} \text{ cm}^2 \text{ V}^{-1} \text{ s}^{-1}$ ($\gamma_{mobility} = 10$),

$\mu_{hole} = 2 \times 10^{-7} \text{ cm}^2 \text{ V}^{-1} \text{ s}^{-1}$ and $\mu_{electron} = 2 \times 10^{-9} \text{ cm}^2 \text{ V}^{-1} \text{ s}^{-1}$ ($\gamma_{mobility} = 100$),

and $\mu_{hole} = 5 \times 10^{-7} \text{ cm}^2 \text{ V}^{-1} \text{ s}^{-1}$ and $\mu_{electron} = 5 \times 10^{-10} \text{ cm}^2 \text{ V}^{-1} \text{ s}^{-1}$ ($\gamma_{mobility} = 1,000$).

.....72

Figure 4.1 (a) Molecular structures of the materials used in organic light emitting diodes (OLEDs). (b; c) Structures of devices 1 and 2 showing the frontier orbital energy levels and thicknesses of the organic materials.

(4s,6s)-2,4,5,6-tetra(9H-carbazol-9-yl) isophthalonitrile (4CzIPN)-doped 3,3-Di(9H-carbazol-9-yl)biphenyl (mCBP),

3',3'''',3''''-(1,3,5-triazine-2,4,6-triyl)tris((1,10-biphenyl]-3-carbonitrile)) (CN-T2T), and 9,10-bis(3-(pyridin-3-yl)phenyl) anthracene (DPyPA) are used as light emitting layer (EML),

triplet/polaron blocking layer, and electron transporting layer.....78

Figure 4.2 (a) Current-density-voltage-luminance, (b) external quantum efficiency-power efficiency-luminance, and (c) luminance-voltage changes

over the duration of the operation (L-V-t) of OLEDs. L-V-t is measured under the constant current condition at an initial luminance of 1,000 cd/m². The driving voltages at 1,000 cd/m² are 4.0 V for device 1 and 4.7 V for device 2.

.....81

Figure 4.3 DC voltage-dependent imaginary Z-frequency spectrums of hole-only half-devices of (a) device 1 and (b) device 2. The transit time of the charge carrier in the charge-only device is determined from the peak frequency of Z"-f spectrums. (c) Field-dependent electron and hole mobilities of hole transporting layers (HTLs) and EMLs. Regarding EML hole mobility, although 100 nm of the EML layer is the same in devices 1 and 2, mobility varies when the HTLs are changed. The dotted lines indicate linear fitting results. (d) Current density-voltage characteristics of charge-only devices consisting of the EML.86

Figure 4.4 (a) Parallel capacitance-voltage at an AC frequency of 50 Hz with current density-voltage-luminance (J-V-L) and (b; c) capacitance-frequencies for various DC voltages of devices 1 and 2. The amplitude of AC voltage is 100 mV. Regarding charge transport in the OLEDs, the capacitance is a result of the total contribution of charge accumulation at the interface, trapping/detrapping responses due to the dopant in the EML, and recombination.....90

Figure 4.5 (a) Capacitance of devices 1 and 2 depending on luminance. (b) Capacitance-frequency of devices 1 and 2 at a luminance of 1,000 cd/m². The driving voltage at 1,000 cd/m² is 4.0 V and 4.7 V for devices 1 and 2,

respectively. (c; d) Schematic illustration showing the transport of electrons and holes in devices 1 and 2 at $1,000 \text{ cd/m}^2$ based on impedance analysis.93

Chapter 1. Introduction

1.1 Electrical doping in organic semiconductors

In the organic electronic devices, enhancement of charge injection and transport is a crucial challenge for device performance because of poor electrical properties of organic semiconductors. Electrical doping is the technology increasing carrier density of organic semiconductors extrinsically via charge transfer by addition of dopants. It has been adopted in a variety of organic electronic devices such as organic light-emitting diodes (OLEDs),^[1-4] organic photovoltaics (OPV),^[5,6] and organic thin-film transistors (OTFTs).^[7,8] However, unlike conventional inorganic semiconductors, carrier density enhanced by doping have not been predicted and controlled. It indicates that charge generation of organic semiconductors is governed by an independent mechanism, which cannot be described using the classical semiconductor theory. Basically, in order to induce the doping effect, dopant has very deep/shallow-lying Fermi level to generate hole/electron in host materials. For *p*-type case, hole density of host increases via the process that electron in highest occupied molecular orbital (HOMO) of the host is transferred to lowest unoccupied molecular orbital (LUMO) of dopant. In organic semiconductors, the process of electrical doping is divided into two fundamental processes, as described in Figure 1.1. After the encounter of host and dopant molecules occurs, charge transfer complex (CTC) is formed due to the Coulomb force

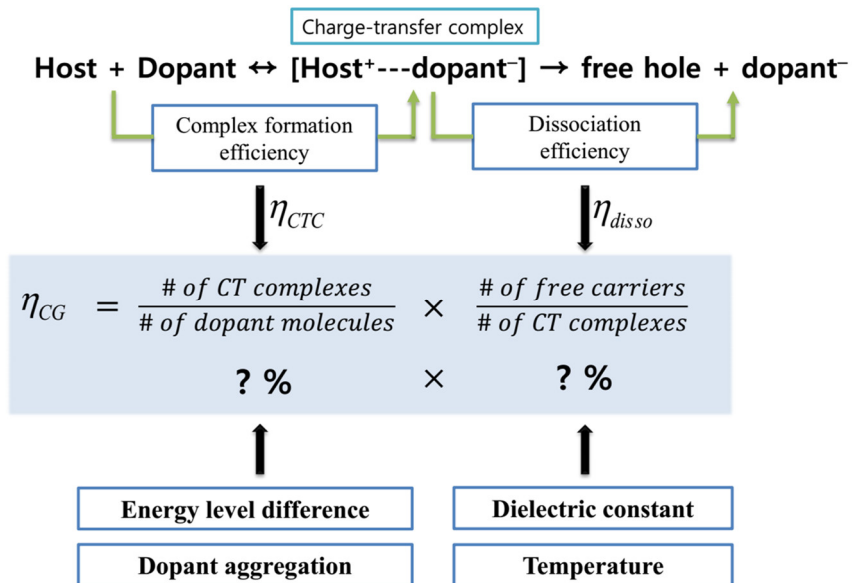
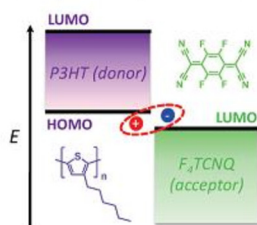


Figure 1.1 Schematic illustration of fundamental processes and main factors of electrical doping in organic semiconductors.

between the ionized state of host and dopant (cationic state of host and anionic state of dopant in *p*-type case). Subsequently, when generated holes of host act as a free carrier by overcoming the binding force of CTC, charge carrier density of host increases. Charge generation efficiency is quantitatively characterized as CTC formation efficiency and dissociation efficiency, respectively. For a comprehensive understanding of doping process of organic semiconductors, distinctive analysis of the CTC and free charge carrier should be performed. The charge generation efficiency of organic semiconductor has been reported to below 10 % in a few mole percent of doping concentration.^[9–13] Therefore, many researches have focused to understand the charge generation of doped organic semiconductors. The formation of the CTC and enhancement of conductivity has been investigated from UV-vis-NIR spectroscopy of doped film and current density-voltage measurement of single carrier devices.^[3,4,11–14] Absorption spectrum of doped film shows additional spectrum in the range of vis-NIR wavelength. It means that energy states are newly formed in the bandgap of host materials via CTC formation. The current density enhancement of single carrier device indicates that conductivity is significantly increased by doping. In addition, the effect of difference of frontier orbital energy between host and dopant on the charge generation efficiency is systematically investigated.^[11,12] Using various hole transporting materials and *p*-type dopants having different frontier orbital energy levels, It is unraveled that the charge generation efficiency increases as the energy level difference of HOMO of host and LUMO (or Fermi level) of dopant increases. Considering that the CTC

is formed via the charge transfer between host and dopant, this finding is interpreted by enhancement of the driving force (energy level difference between host and dopant) to the charge transfer. As one of the factors affecting to the charge generation efficiency, dispersion property of dopant has been reported.^[13,14] Investigation using transmission electron microscopy and UV-Vis-NIR spectroscopy reveals that metal oxide dopant such as rhenium oxide or molybdenum oxide has high aggregation property compared to organic dopant. According to the aggregation property, the charge generation efficiency of organic dopant (tris[1,2-bis(trifluoromethyl)ethane-1,2-dithiolene]) is higher than metal oxide dopants in NPB host. These reports contribute to understand the charge generation process of doping and gives physical insight to enhance the effectiveness of electrical doping. To unravel mechanisms underlying the nature of the doping process, involving the formation of CTC and generation of charge carrier, two mechanisms are suggested at present.^[9,10,15,16] Figure 1.2 shows main concepts of integer charge transfer (ICT) model and hybrid CTC model. In the ICT model, charge transfer between host and dopant is interpreted as an integer charge transfer. After the charge transfer, ionized host and dopant form the CTC. Although this state is named as a kind of complex, the CTC is considered as bound state of independent host and dopant molecules in the ICT model. In addition, the requirement for the charge transfer is that the difference between frontier orbital energy between host and dopant should be higher than zero. In contrast, the hybrid CTC model considers chemical nature of organic semiconductors. The

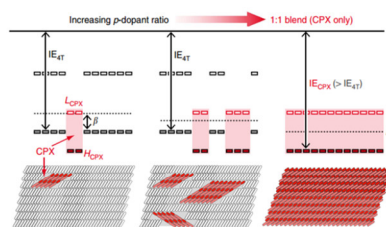
ICT model (Integer charge transfer)



$$\Delta E > 0$$

- Integer charge transfer between host and dopant molecules.
- Coulomb binding force induced by ionized dopant is main reason for low doping efficiency.

Hybrid CTC model



$$\Delta E < 0 \text{ or } \approx 0$$

- Hybrid frontier orbital between host and dopant molecule is formed.
- Reorganization of energy level is proposed.

Figure 1.2 Schematic diagram of charge generation mechanisms in electrically doped organic semiconductors.

charge transfer is considered as an electron transfer between localized orbital in a moiety of molecules. Therefore, the CTC can be formed if the energy difference is not higher than zero. After the charge transfer, electronic structure of the CTC is totally changed through orbital reorganization of the CTC. An increase of carrier density in the host is interpreted that the occupation possibility at LUMO increases through Fermi level alignment between host and CTC. From the evidence supporting two mechanisms experimentally, charge generation of doped organic semiconductors is not governed by single mechanism only. Meanwhile, the charge transport in doped organic semiconductors has been a critical research topic in addition to charge generation. From hole only devices and metal-insulator-semiconductor (MIS) device consisting of ReO₃ doped 4,4',4''-tris(N-(2-naphthyl)-N-phenyl-amino)-triphenyl amine (2-TNATA), doping concentration-dependent hole mobility is investigated.^[17] A decrease of hole mobility with increasing doping concentration is attributed to the Coulomb trap which is formed from ionized dopants. Activation energy of conductivity shows an increase as doping concentration increases. It is interpreted that the Gaussian distribution of density of states is broadened by the production of deep trap states. In further research with various host and dopants, the density of states distribution and mobility in doped organic semiconductors are systematically investigated.^[18] For all combination of host and dopants investigated, the hole mobility in 5 mol% doped organic semiconductors show 10⁻⁷-10⁻⁶ cm²/Vs. It indicates that the ionized dopants act as an electrical trap to generated free charge carriers. Above

5 mol% of doping concentration, increase or decrease of hole mobility depending on doping concentration is understood by the correlation between the Coulomb trap depth and energetic disorder of host materials. The Coulomb trap depth due to ionized dopants decreases with doping concentration since overlap of the Coulomb potentials became large. Decreasing energy barriers due to the Coulomb potentials became equal or smaller than equilibration energy of the host at higher doping concentration. When the equilibration energy is higher than the Coulomb potentials, all generation carrier freely transport without trapping due to the ionized dopants. Therefore, the charge carrier mobility increases with doping concentration. For the doping concentration region which equilibration energy is lower than the Coulomb potentials, the charge carrier mobility decreases with doping concentration as the charge transport is retarded by the Coulomb trap. The theoretical and experimental investigations of the charge carrier mobility in doped organic semiconductors gives better understanding of microscopic process of the charge transport under the co-existence of generated free charge carrier and ionized dopant in amorphous organic semiconductors.

1.2 Operational stability of OLEDs

1.2.1 Organic light-emitting diodes

Organic light-emitting diodes are light-emitting diode consisting of organic semiconductors firstly reported by C. Tang at 1987.^[19] During thirty years after that, a great advance has been realized in terms of light-emitting efficiency and device stability with comprehensive research and development of researchers.^[20–23] Based on the advances, OLEDs has been successfully commercialized as a practical display for mobile phone, television, automobile, and general lighting as shown in Figure 1.3. OLED has extended application field gradually, which conventional liquid crystal display is used in. Figure 1.4 displays device structure of OLEDs. OLEDs are made of a multilayer of organic layers serving as a charge transporting layer, light-emitting layer, charge/exciton blocking layer, and so on. Electrons and holes injected from electrodes recombine in the light-emitting layer and light is out-coupled toward transparent electrodes. Theoretically, the external quantum efficiency (EQE) of OLEDs is described by

$$\eta_{EQE} = \gamma \times \eta_{S/T} \times \varphi_{eff}(\varphi_{PL}, \Theta, \Gamma) \times \eta_{out}(\Theta, \Gamma) \quad (1.1)$$

where γ , $\eta_{S/T}$, φ_{eff} , φ_{PL} , Θ , Γ , and η_{out} are the charge balance factor, the singlet-triplet factor (0.25 for fluorescent, 1 for phosphorescent and thermally activated delayed fluorescent (TADF) emitters), the effective quantum yield, the photoluminescence (PL) quantum yield, the horizontal dipole ratio, the

(a)



(b)



(c)



Figure 1.3 Commercial products adopting organic light-emitting diodes. (a) Samsung Galaxy S8 (b) Apple iPhone X (c) LG Signature TV.

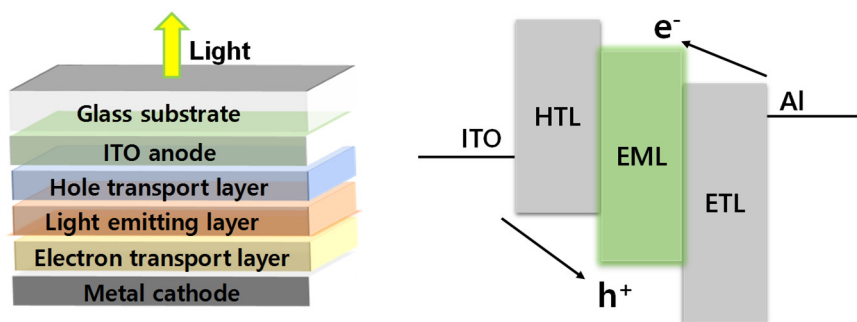


Figure 1.4 Schematic diagram of charge generation mechanisms in electrically doped organic semiconductors.

geometric factor of the device, and the out-coupling efficiency, respectively. The effective quantum yield and the out-coupling efficiency are affected by the geometric factor of the device which considers the optical microcavity structure of the device as the Purcell factor.

1.2.2 Operational stability of organic light-emitting diodes

In order to utilize OLEDs as a practical display, the device lifetime of the device should be long at the luminance of $100 \sim 400 \text{ cd/m}^2$. With an efficiency enhancement, many researches have focused on elucidating degradation mechanism and finding a way to improve the operational stability via the novel design of materials and devices.^[24-27] Figure 1.5 describes the history of an operational lifetime of OLEDs in terms of half lifetime which is the time that luminance decreases to 50% of initial luminance. For all colors, fluorescent devices are more stable than phosphorescent devices since exciton lifetime of fluorescence is short (\sim ns). In case of phosphorescent devices, the device lifetime of red and green-emitting devices increases considerably compared to blue devices. A relatively short lifetime of blue emitting devices is caused by large exciton energy resulting bond dissociation. In commercial products, red and green pixels adopt phosphorescent devices and blue pixel still uses fluorescent devices due to the device lifetime. Therefore, enhancement of blue phosphorescent device has been considered as a challenge. Meanwhile, TADF emerged as an efficient fluorescent emitting mechanism which can harvest

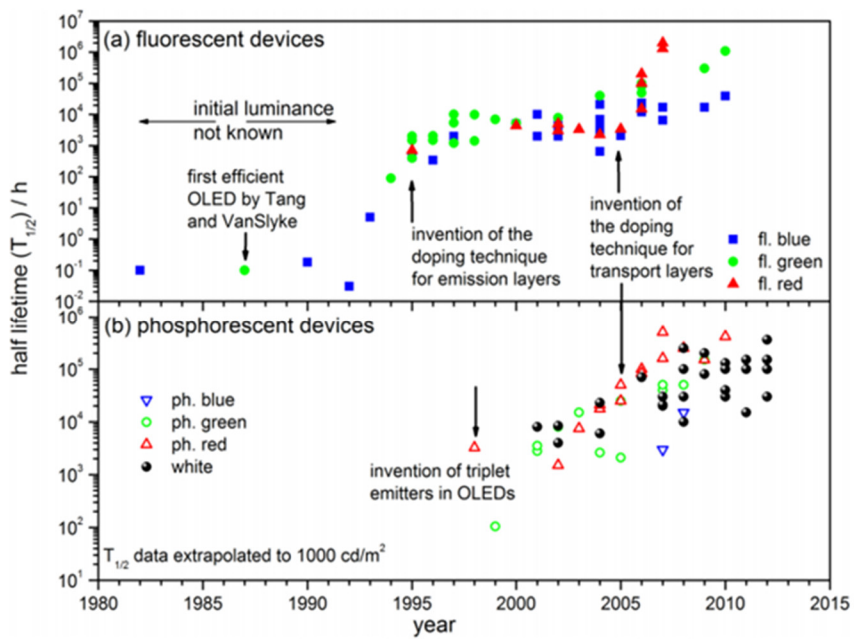


Figure 1.5 History of device lifetime of fluorescent and phosphorescent OLEDs.^[26]

triplet excitons via reverse intersystem crossing.^[28] TADF dopant does not include heavy metal atom and synthesis is easier than phosphorescent dopant. Consequently, OLEDs adopting TADF mechanism is considered as a third-generation device and device lifetime of TADF devices has been investigated recently.^[29–33] Figure 1.6 shows degradation mechanism of OLEDs including internal and external origins. In principle, degradation of OLEDs is caused by bond dissociation of organic materials. In case of intrinsic origins, since electrons and holes are injected from the electrodes and recombine at the EML, there are degradation reactions related with exciton and polaron. Exciton and polaron independently induce material degradation and interaction between polaron and exciton is reported to accelerate degradation reaction. Therefore, control of exciton and polaron is important to retard degradation of OLEDs. In terms of device physics, exciton density, charge balance, recombination zone, and polaron accumulation are closely related to device lifetime. As an external degradation mechanism, there are environmental origins involving the existence of oxygen, water, and impurity, fabrication-related parameters, and driving temperature, and so on. These origins result in the catastrophic failure and the change of morphology of OLEDs. It indicates that stable OLED is possible by carefully established fabrication condition.

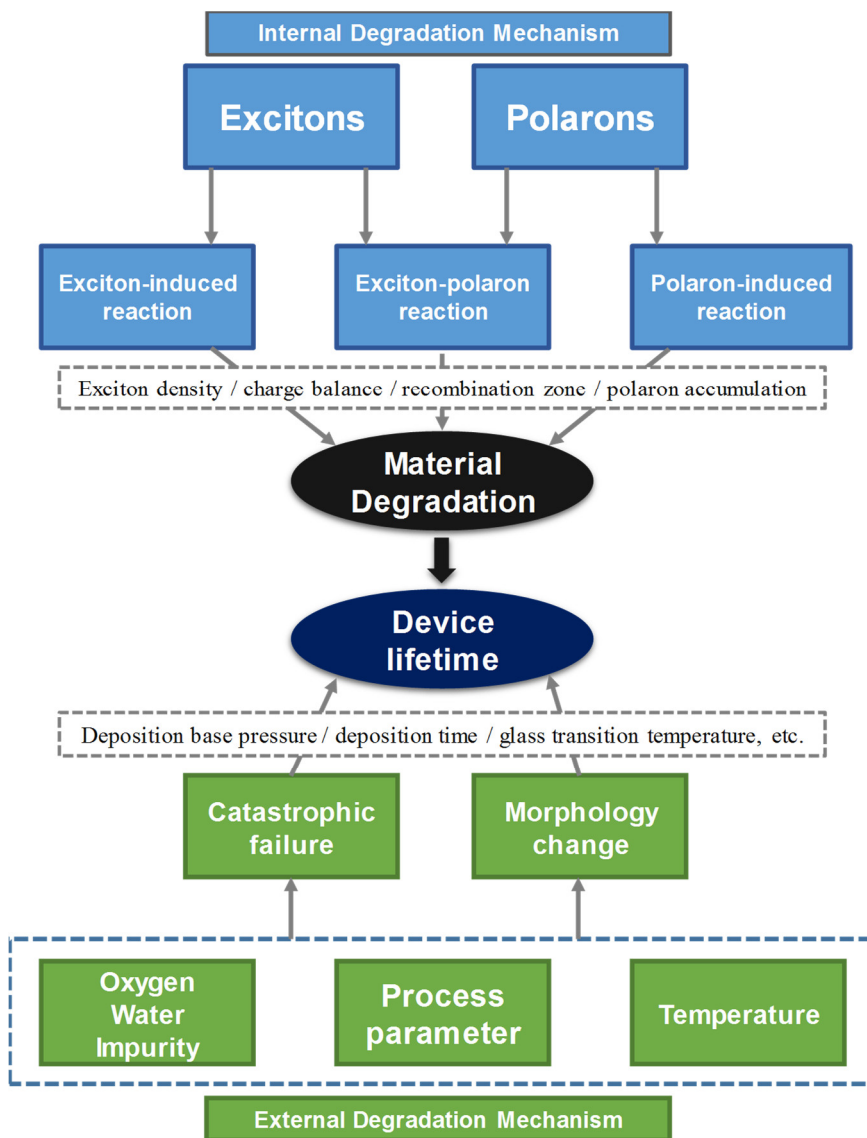


Figure 1.6 Internal and external degradation origins of organic light-emitting diodes

1.3 Theoretical description of electrical characteristic of OLEDs (Drift-diffusion numerical modeling)

1.3.1 Introduction

For a fundamental understanding of the charge behavior in OLEDs during operation, drift-diffusion numerical modeling is performed. Since electrons and holes transport toward the EML and recombination inside the multilayer structure, theoretical description of these processes needs to be established. In this chapter, governing equations of drift-diffusion numerical modeling will be addressed. As a bulk numerical model, charge transport is described as a combination of drift and diffusion mechanisms. For charge transport at the organic-organic heterointerface, thermally assisted transport model is used. Recombination phenomena are described by both Langevin recombination and trap-assisted recombination mathematically. Finally, the assumption and corresponding limitation of the simulation are addressed.

1.3.2 Bulk charge transport: drift and diffusion model

The goal of drift-diffusion modeling is to simulate the local distribution of charge density, electric field, recombination zone, and so on. For the objective, the equations correlating these properties should be established. In the semiconductor, charge transport is governed by both electric field induced drift and concentration-driven diffusion mechanism. Diffusion induced transport

can be expressed by the Einstein relation. In addition, distribution of charge density is related to electric potential as the Poisson relationship. Totally, time-dependent charge density and electric potential are correlated by Poisson relation, drift-diffusion charge transport, and recombination as follows.

$$\frac{\varepsilon_0 \varepsilon_r}{q} \frac{\partial^2 \varphi(x,t)}{\partial x^2} = p(x,t) - n(x,t) + N_D - N_A + \sum \rho_t(x,t) \quad (1.1)$$

$$\frac{\partial p(x,t)}{\partial t} = \frac{1}{q} \frac{\partial}{\partial x} \left[-\frac{\mu_p kT}{q} \frac{\partial p(x,t)}{\partial x} - \mu_p p(x,t) E(x,t) \right] + R(x,t) \quad (1.2)$$

ε_0 , ε_r , q , φ , p , n , N_D , N_A , ρ_t , E , and R are the vacuum permittivity, dielectric permittivity, electronic charge, electric potential, hole density, electron density, ionized donor density, ionized acceptor density, trapped charge, electric field, and recombination term, respectively. Ionized donor and acceptor densities in the Poisson equation are included for electrical doping of charge transport layer. Recombination term in time-dependent charge density equation will be addressed later. In the numerical simulation, the charge density and the electric potential are independent solution values in the differential equations.

1.3.3 Charge transport at interface: thermionic emission model

Since the OLEDs is composed of a multilayer of organic semiconductors, there are a few of energetic barriers, which is frontier orbital energy difference

between adjacent two layers. In the numerical simulation, the charge transport across the energetic barrier is modeled by thermally assisted emission. The carrier density at the interface is described by

$$p(x_n) = p(x_{n-1}) \exp\left(-\frac{|\Delta E|}{k_B T} \delta(\Delta E)\right) - p(x_n) \exp\left(-\frac{|\Delta E|}{k_B T} \delta(-\Delta E)\right) \quad (1.3)$$

$$\delta(\Delta E) = \begin{cases} 1 & (\Delta E > 0) \\ 0 & (\Delta E \leq 0) \end{cases}$$

where ΔE and $\delta(\Delta E)$ are the difference of frontier orbital energy between layers and mathematical component to reflect the case that energetic barrier does not exist at the interface. The thermionic emission equation is considered as a boundary condition in the numerical modeling.

1.3.4 Recombination: Langevin and trap-assisted models

In the EML, recombination occurs via two kinds of mechanisms, which are Langevin (direct) and trap-assisted (indirect) recombination. Langevin recombination indicates band-to-band recombination of electron and hole in a single molecule. The single molecule can be host or dopant molecule in the EML. In case of OLEDs, the molecule where the Langevin recombination occurs is considered as a host molecule since the density of state of the host is larger than dopant. Recombination via Langevin mechanism is dependent on charge mobility and described as follows.

$$R_{Langevin} = r_{Langevin} n(x) p(x) = \frac{q}{\varepsilon} (\mu_e + \mu_h) n(x) p(x) \quad (1.4)$$

$r_{Langevin}$, μ_e , and μ_h are recombination coefficient and charge mobility of electron and hole, respectively. According to the equation, the rate of Langevin recombination is proportional to the charge mobilities of electron and hole. As a second mechanism, trap-assisted recombination is a recombination that trapped charge participate in. In the host-dopant system of the EML, the dopant is considered as an electrical trap when one of frontier orbital energy levels of dopant is located inside bandgap of the host. Therefore, in the EML, the charges exist both host orbital and trap energy state (orbital of dopant). In order to consider the recombination via trapped charge, additional theoretical description is needed. For the trap density $N_t(E)$ with the energetic distribution $f_t(E, x)$, the capture coefficient and the emission rate are expressed by following equations according to classical semiconductor theory.

$$c_{n,p} = v_{n,p} \sigma_{n,p} \quad (1.5)$$

$$e_n(E, x) = c_n N_C e^{-(E_C - E)/kT} \quad (1.6)$$

$$e_p(E, x) = c_p N_V e^{-(E - E_V)/kT} \quad (1.7)$$

$c_{n,p}$, $v_{n,p}$, $\sigma_{n,p}$, $e_{n,p}(E, x)$, $N_{C,V}$, and $E_{C,V}$ are capture coefficient, charge velocity, capture cross-section, emission rate, the density of state, and frontier orbital energy levels, respectively. From the capture and emission coefficient, trap-assisted recombination is derived from the trap-detrap dynamics.

$$R_n^{trap-assist} = \int c_n n(x) N_t(E) (1 - f_t(E, x)) - e_n(E, x) N_t(E) f_t(E, x) dE \quad (1.8)$$

$$R_p^{trap-assist} = \int c_p p(x) N_t(E) f_t(E, x) - e_p(E, x) N_t(E) (1 - f_t(E, x)) dE \quad (1.9)$$

In this work, trap energy levels (dopant level in the EML) is assumed to be single level corresponding to the frontier orbital energy level of dopant.

1.3.5 Assumption and corresponding limitation of simulation

In the drift-diffusion simulation, since fundamental components of the differential equations are adopted from the classical semiconductor model, there are a few points which do not reflect the nature of the organic semiconductors. First of all, HOMO and LUMO are considered as the conduction and valence band which have the density of states at the single energy level. However, frontier orbital energy states of the organic semiconductor are characterized by a Gaussian distribution. The equation for the organic-organic interface should be modified to reflect the charge transport between the distributed density of state. In addition, since the factors characterizing Gaussian distribution are different in each organic materials, experimentally obtained values should be included. Second, some values in the recombination equation are ideally calculated. Given a variety of moieties in the organic molecules of the EML, it can be deduced that the recombination coefficient depends on the molecular structure of host and dopant. Moreover, the recombination coefficient of exciplex-forming co-host is thought to be

larger than single host because of the binding force between electron donor and acceptor of each host materials. In the simulation, band-to-band recombination is described by the Langevin relationship involving the charge mobility as the factor only. Similarly, trap dynamics in trap-assisted recombination does not reflect the chemical nature of the organic semiconductors. Third, ideal injection barrier of 0.3 eV in the simulation should be modified to consider real value. The charge injection between charge transport layer and the metal electrode is dependent on not only the difference of energy levels but also the charge injection materials and electrical doping.

For minimizing these assumptions in the simulation, further research should be performed to establish the experimental methods for characterizing microscopic processes in OLEDs quantitatively.

1.4 Impedance spectroscopy

1.4.1 Introduction: fundamental theory

Impedance spectroscopy is a powerful tool for analyzing dynamic characteristics of organic semiconductors and OLEDs. During measurement, since oscillating voltage with DC component is applied to sample, physical understanding of electrical theory under static state should be extended to time-dependent dynamic state.

Impedance is the resistance under alternating voltage environment. It is expressed by complex form because of DC and AC component. In order for intuitive understanding of fundamental concepts, a single capacitor is assumed as circuit model to derive mathematical description. For a single capacitor, time-dependent voltage and current is given by

$$V(t) = V \sin(\omega t), \quad I(t) = C \frac{\partial V(t)}{\partial t} \quad (1.10)$$

where ω is the angular frequency of oscillating voltage. Impedance is derived as follows.

$$Z = \frac{V(t)}{I(t)} = \frac{V \sin(\omega t)}{C \omega V \cos(\omega t)} = \frac{\sin(\omega t)}{\omega C \sin\left(\omega t + \frac{\pi}{2}\right)} = \frac{1}{\omega C} e^{-j\frac{\pi}{2}} = \frac{1}{j\omega C} \quad (1.11)$$

$$e^{j\left(-\frac{\pi}{2}\right)} = \cos\left(-\frac{\pi}{2}\right) + j \sin\left(-\frac{\pi}{2}\right) = -j \quad (\text{Euler's formula})$$

In another form, admittance, defined as reciprocal of impedance, is given by

$$Y = \frac{1}{Z} = j\omega C = \frac{j\omega A \epsilon_0 (\epsilon_r' - j\epsilon_r'')}{d} = \frac{\omega \epsilon_0 \epsilon_r'' A}{d} + j \frac{\omega \epsilon_0 \epsilon_r' A}{d} \quad (1.12)$$

$$Y = G + jB \quad (1.13)$$

where ϵ_r' , ϵ_r'' , A , and d are real and imaginary dielectric constant, area of dielectric plate and distance of capacitor. Admittance is expressed by complex form. Real part and imaginary part of admittance are called as conductance G and susceptance B , respectively. According to above equations, conductance involves imaginary permittivity and susceptance contains real permittivity. In Figure 1.7, schematic description of dielectric loss mechanism of materials is depicted. Frequency-dependent complex dielectric constant gives a knowledge of various polarization mechanisms in dielectric material. Therefore, a variety of dynamic properties depending on dielectric loss mechanism can be determined by analyzing admittance response. In the field of the organic electronics, capacitance induced from impedance is analyzed instead of conductance or susceptance for intuitive understanding charge behavior. The capacitance can be derived as a series form or a parallel form according to equivalent circuit. Since organic semiconductor is treated as a parallel resistance-capacitance (RC) circuits, the capacitance usually indicates parallel capacitance derived from impedance. Impedance of parallel RC circuit is derived by

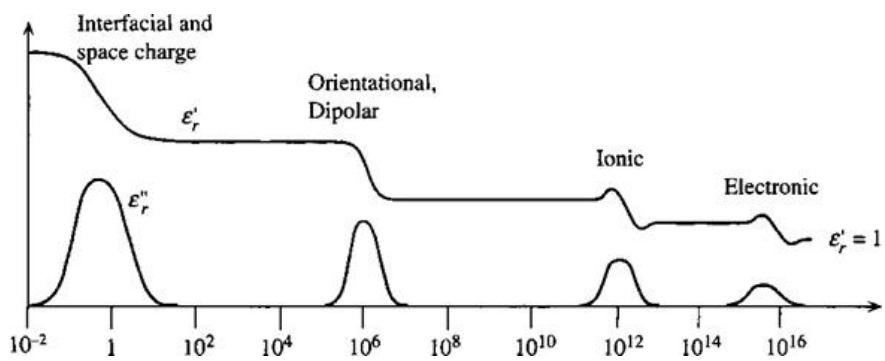


Figure 1.7 Schematic diagram of dielectric loss mechanism of materials depending on frequency in view of complex dielectric permittivity.

$$\frac{1}{Z} = \frac{1}{R} + \frac{1}{-jX_C} = \frac{-jX_C + R}{R(-jX_C)} \quad (1.14)$$

$$\frac{1}{Z} = \frac{1}{R} + j\frac{1}{X_C} \quad (1.15)$$

$$|Z|^2 = \frac{X_C^2 R^2}{X_C^2 + R^2} \quad (1.16)$$

$$Z = \frac{RX_C}{X_C + jR} = \frac{RX_C(X_C - jR)}{X_C^2 + R^2} = \frac{RX_C^2}{X_C^2 + R^2} - j\frac{R^2 X_C}{X_C^2 + R^2} \quad (1.17)$$

where X_C is reactance of capacitance. Therefore, the correlation between complex impedance and parallel capacitance is expressed by

$$\frac{-\text{Im}(Z)}{2\pi f |Z|^2} = \frac{\frac{X_C R^2}{X_C^2 + R^2}}{2\pi f \left(\frac{X_C^2 R^2}{X_C^2 + R^2} \right)} = \frac{1}{2\pi f X_C} = \frac{2\pi f C_p}{2\pi f} = C_p \quad (1.18)$$

where $X_C = \frac{1}{2\pi f C}$.

In this research, the capacitance in the experiment is derived from Z' and Z'' according to the relation.

1.4.2 Carrier density in electrically doped organic semiconductors from Mott-Schottky analysis

Quantitative analysis of free carrier density of doped organic semiconductor is crucial to determine the doping efficiency of dopant. Using impedance spectroscopy, carrier density can be measured by the Mott-Schottky analysis. The Mott-Schottky method analyzes capacitance-voltage originating from the change of depletion layer due to charge injection and extraction. Therefore, in an electronic device, only single carrier should be injected and extracted from the electrode. In order to block counterpart charge from the electrode, insertion of insulator or formation of the Schottky barrier is designed. In this thesis, metal-insulator-semiconductor (MIS) device is fabricated and device structure is depicted in Figure 1.8(a). In MIS device, capacitance changes depending on voltage since depletion width is changed because of charge injection. The correlation between carrier density and voltage-dependent capacitance is given by

$$N_{free-carrier} = \frac{2}{q\epsilon_0\epsilon_r} \frac{\partial C_p^{-2}}{\partial V} \quad (1.19)$$

$N_{free-carrier}$, q , ϵ_0 , ϵ_r , C_p , and V are carrier density, elementary charge, vacuum permittivity, dielectric constant, parallel capacitance, and voltage, respectively. Figure 1.8(b) shows $1/C^2$ - V characteristics called as Mott-Schottky plot. The slope of $1/C^2$ - V in transition regime is determined to calculate the carrier density. Figure 1.8(c) depicts capacitance loss spectrum (G/ω). In the

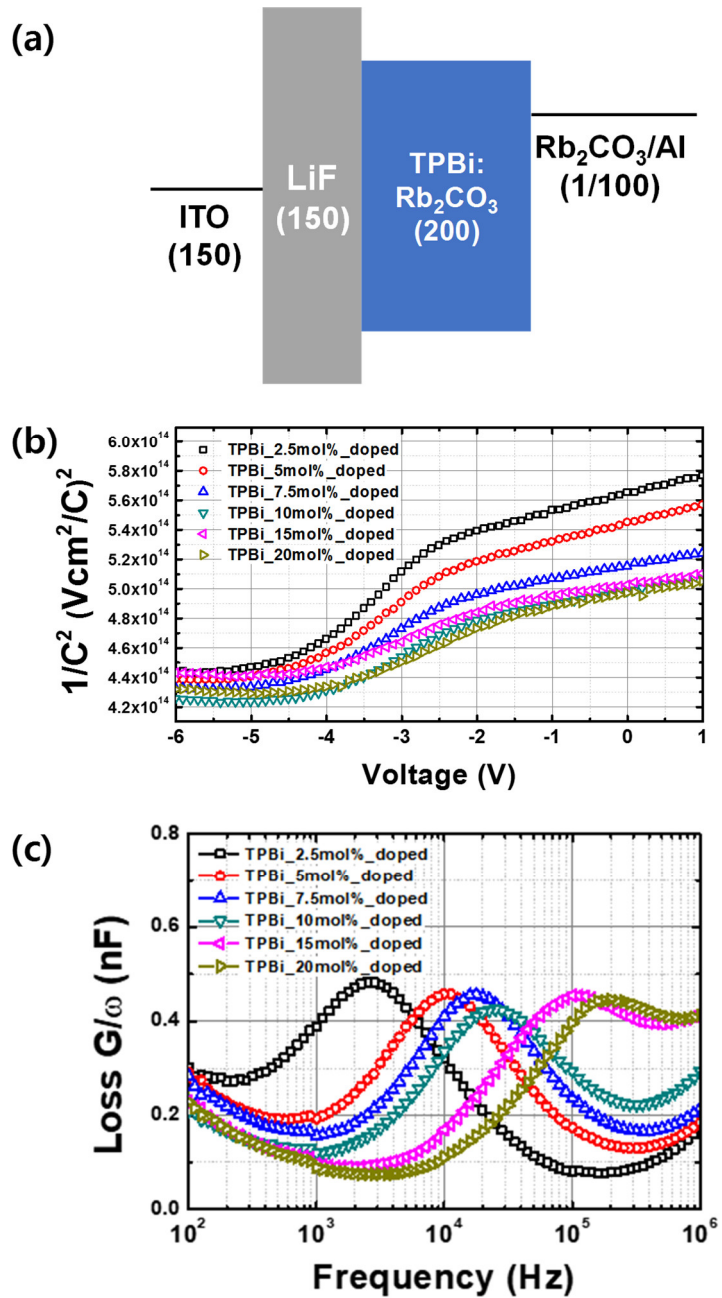


Figure 1.8 (a) Device structure of metal-insulator-semiconductor (MIS) devices (b) Mott-Schottky plot ($1/C^2$ -V) of MIS devices (c) capacitance loss spectrum.

measurement of capacitance-voltage, determination of AC frequency is important since charge carriers in organic semiconductor should follow oscillating voltage. The peak of loss spectrum indicates the dielectric loss due to non-response of carriers. Therefore, the frequency in the measurement should be lower than the peak frequency of the capacitance loss spectrum.

1.4.3 Field-dependent mobility from $-AB$ and $Im Z$ method

Utilizing the dielectric loss due to charge carrier in the organic semiconductors, field-dependent mobility can be measured using impedance spectroscopy. To determine mobility, the transit time of charge carriers should be derived from a real and imaginary component of impedance. According to the analyzed parameter, there are two methods in mobility analysis, $-AB$ and $Im Z$ method as shown in Figure 1.9.^[34-39] For $-AB$ method, $-AB$ means a negative differential difference of susceptance, which includes real dielectric permittivity. In case of $Im Z$ method, imaginary Z is used to determine the transit time. For both methods, the spectrum shows a peak at the frequency that dielectric loss occurs. Charge carrier mobility is derived from the transition (characteristic) frequency as follows.

$$f_{\max} = \kappa \frac{1}{\tau_{tr}} \quad (1.20)$$

$$\mu = \frac{d^2}{\tau_{tr} V} \quad (1.21)$$

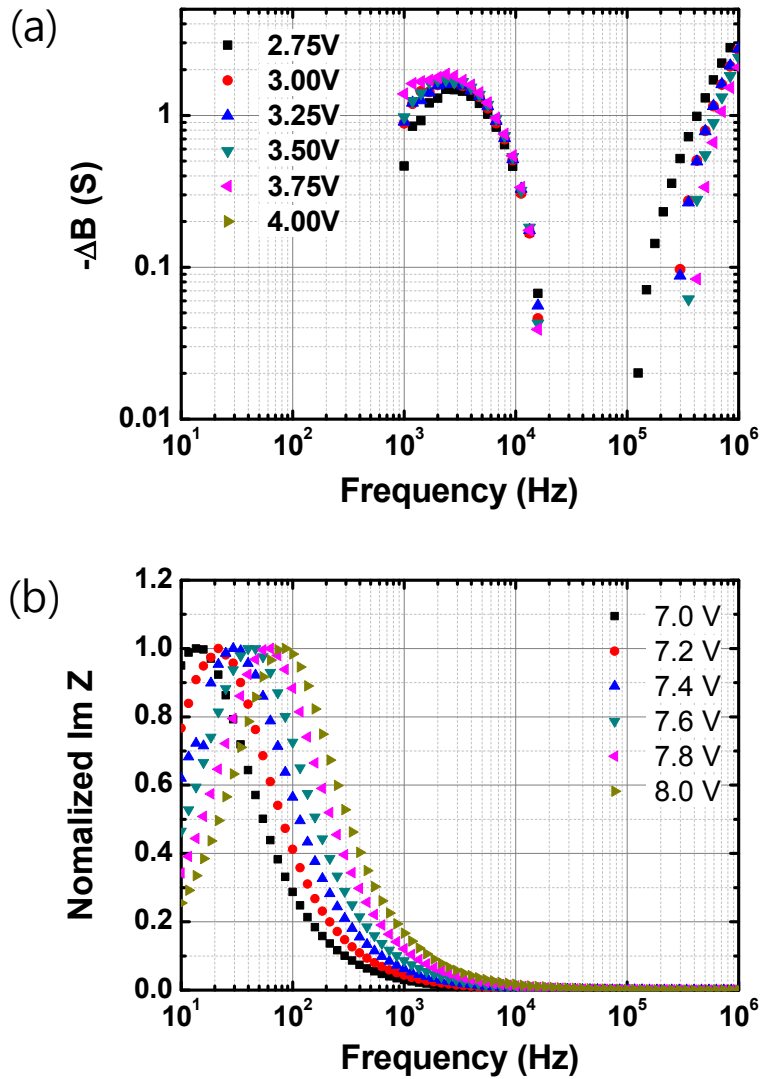


Figure 1.9 (a) Negative differential susceptance ($-\Delta B$) spectrum and (b) imaginary Z spectrum of a single carrier device for various DC voltages.

f_{max} , κ , and τ_{tr} are transition frequency, numerical coefficient, and transit time, respectively. The numerical coefficient can be determined from simulation (drift-diffusion numerical modeling or analytic SCLC modeling) or experiment (space-charge-limited current or time-of-flight method).^[36,37] Compared to time-of-flight method, the layer thickness of the organic materials is not needed to be thick as 1000 nm and the measurement is performed under carrier injected condition, which is the same environment with OLEDs operation.

1.4.3 Impedance analysis of OLEDs

From a steady-state electrical characterization like the current density measurement, dynamic characterization of OLEDs is not obtained. Using the impedance spectroscopy, dynamic properties of the charge transport in OLEDs can be analyzed since oscillating voltage is additionally applied to the device. Given the frontier orbital energy levels of multilayer structure of OLEDs, capacitance of OLEDs is affected by several mechanisms. Figure 1.10 depicts the origin of capacitance characteristic of OLEDs correlated with the charge transport. First, charge accumulation at the interface between organic layers increases capacitance.^[40-42] With an increase of voltage, the charge accumulation occurs due to difference of charge carrier mobility or frontier orbital energy level between adjacent two organic layers. The knowledge of the charge accumulation from experimental analysis clearly enables to confirm the speculation which is deduced from the frontier orbital energy levels of each

$$C_p = C_{accumulation} + C_{trap-detrapped} + C_{recombination}$$

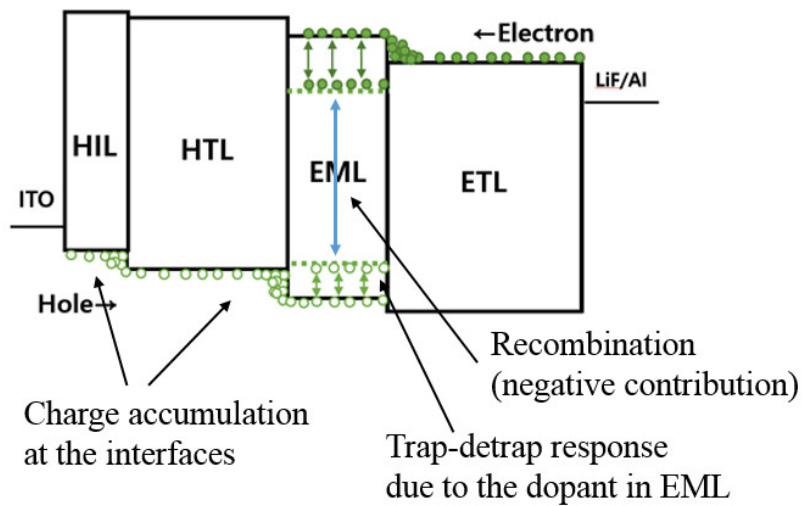
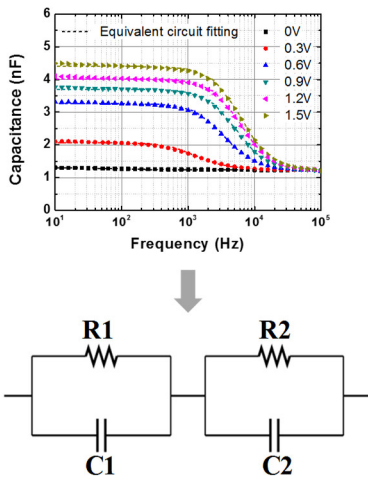


Figure 1.10 Schematic description of mechanisms contributing the capacitance of OLEDs.

layer. Second, trap-detrap of the charge increases capacitance.^[43–46] Trap states exist in the bandgap of organic layers because of an impurity materials or emitting dopant in the EML. For OLEDs adopting host-dopant structure in the EML, at least one of the frontier orbital energy levels of the emitting dopant is located in the bandgap of the host. Therefore, the emitting dopant is energetically electrical trap for the charges in the host. Usually, as doping concentration of the dopants is higher than amount of the impurity, an increase of capacitance is mainly induced from the emitting dopant in the case. Third, recombination in the EML results in a capacitance decrease. It is rationalized by extinction of the charges via exciton formation. However, interestingly, some cases of OLEDs show negative capacitance with increasing driving voltage in many reports.^[40,42,47–50] Although this phenomenon has been discussed with the recombination, detail correlation between negative capacitance and the recombination in view of the charge dynamics is still not unraveled.^[47–50] During operation of OLEDs, these three mechanisms simultaneously contribute capacitance. Therefore, the origins of capacitance of OLEDs should be understood in view of these processes. In order to clarify the mechanisms separately, capacitance-frequency (C-f) characteristic is analyzed. Figure 1.11 shows C-f characteristics according to underlying mechanisms. In case of capacitance induced by the charge accumulation mechanism, C-f shows plateau shapes with transition frequency. It is attributed that accumulated charges react with oscillating voltage under transition frequency corresponding to the transit time of the charges. In equivalent circuit model, it is also

Charge accumulation at the interfaces



Trap-detrap response

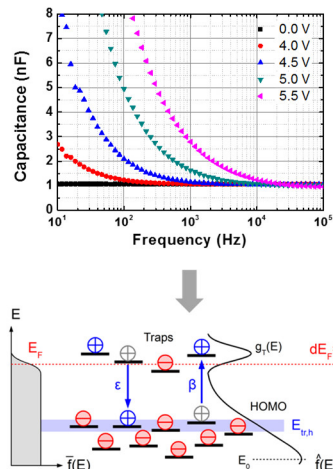


Figure 1.11 Schematic description of principle of charge accumulation and trap-detrap response induced capacitance-frequency spectrums.

understood that highly resistive RC circuit is additionally exists since the retardation due to the energetic barrier or mobility is considered as a resistor. For the case of capacitance induced by the trap-detrap of the charges, the capacitance increases with a decrease of frequency. In organic semiconductors, the frontier orbital energy states have Gaussian distribution. As frequency decreases, trap-detrap response between energetically deeper states are activated because of short transit time, resulting in the capacitance increase.

1.4.4 Theoretical description of the impedance of trap response

In this section, the capacitance induced from trap response is theoretically described.^[43] This model assumes the Boltzmann statistic and energetic distribution of trap states in organic semiconductors. In case of electron traps, free electron in the conduction band, trapped electrons, and the trap occupation probability are expressed by

$$n_c = N_c \exp\left(\frac{E_F - E_C}{kT}\right) \quad (1.22)$$

$$n_t = \int_{E_V}^{E_C} g(E) f_t(E) dE \quad (1.23)$$

$$f_t(E) = \left[1 + \exp\left(\frac{E - E_F}{kT}\right) \right]^{-1} \quad (1.24)$$

where n_c , N_c , E_F , E_C , k , T , n_t , $g(E)$, and $f_t(E)$ are free charge carrier, effective density of state, Fermi level, conduction level, Boltzmann constant,

temperature, trap distribution, and trap occupation probability, respectively.

Trap-detrap kinetics can be described by differential equation as follows.

$$\frac{\partial n_c}{\partial t} = -\frac{\partial n_t}{\partial t} = \int_{E_V}^{E_C} g(E) \frac{\partial f_t(E)}{\partial t} dE \quad (1.25)$$

$$\frac{\partial f_t(E)}{\partial t} = \beta n_c [1 - f_t(E)] - \varepsilon f_t(E) \quad (1.26)$$

β and ε are the capture and release coefficient of the traps. When considering AC components, DC values and AC values are expressed as x_{dc} and x_{ac} . Applying steady-state condition to equation (1.26) gives

$$f_{t,dc} = \left[1 + \exp\left(\frac{E_t - E_F}{kT}\right) \right]^{-1} = \left(1 + \frac{\varepsilon}{\beta n_{c,dc}} \right) \quad (1.27)$$

$$\varepsilon = \beta N_C \exp\left(\frac{E_t - E_C}{kT}\right) \quad (1.28)$$

Then the capacitance due to trap response is given by

$$C_{trap}(\omega) = \frac{Y(\omega)}{j\omega} = \frac{q}{V_{ac}} n_{t,ac} = \frac{q}{V_{ac}} \int_{E_V}^{E_C} g(E) f_{t,ac}(E) dE \quad (1.29)$$

The trap occupation probability with small signal perturbation is approximated to

$$f_{t,ac}(E) = \frac{1}{n_{c,dc}} \frac{f_{t,dc}(E) [1 - f_{t,dc}(E)]}{1 + j\omega / \omega_t} n_{c,ac} = \frac{q}{kT} \frac{f_{t,dc}(E) [1 - f_{t,dc}(E)]}{1 + j\omega / \omega_t} V_{ac} \quad (1.30)$$

$$\omega_t = \frac{\mathcal{E}}{1 - f_{t,dc}(E)} \quad (1.31)$$

where ω_t is characteristic frequency of the trap. Finally, capacitance induced from trap response is

$$C_{trap}(\omega) = \frac{Y(\omega)}{j\omega} = \frac{q^2}{kT} \int_{E_V}^{E_C} \frac{f_{t,dc}(E) [1 - f_{t,dc}(E)]}{1 + j\omega / \omega_t} g(E) dE \quad (1.32)$$

Therefore, the capacitance-frequency characteristics originating from trapping and de-trapping is theoretically described on the basis of the classical semiconductor model.

Chapter 2. N-Type Molecular Doping in Organic Semiconductors: Formation and Dissociation Efficiencies of a Charge Transfer Complex

2.1 Introduction

Electrical doping is widely used to enhance the conductivity of organic semiconductors by increasing charge carrier density. However, doping characteristics of organic semiconductors are different from inorganic semiconductors because of intrinsic properties which include Gaussian density of states, charge transfer process of molecular doping, low dielectric constant, and so on.^[10,51] Two different models have been proposed to describe the electrical doping in organic semiconductors: the integer charge transfer model and the orbital hybridization model.^[15,52,53] In the integer charge transfer model, doping generates free charge carriers through integer charge transfer between host and dopant molecules. The ionized dopants and free carriers are generated simultaneously and, since they have an opposite polarity, the ionized dopants act as Coulomb traps to the free carriers.^[17] The low charge generation efficiency in OSs compared to inorganic semiconductors can be attributed to a strong Coulomb binding energy, because common organic semiconductors have a low dielectric permittivity of about 3.^[54] In contrast to the integer charge transfer model, the orbital hybridization model states that the doping effect is

caused by the formation of hybrid charge transfer complexes upon partial charge transfer between host and dopant molecules.^[52,53] In this model, the doping property originates from the hybrid charge transfer complex which has narrow band gap. As a result of the difference between the Fermi energy level and the unoccupied states of hybrid charge transfer complexes, only a fraction of hybrid charge transfer complexes can be ionized at room temperature resulting in low charge generation efficiency. It is also reported that dopant aggregation^[13,14] and low dissociation probability related to the disorder at the transport level^[55] are other factors that cause low charge generation efficiency. Recently, the modified Fermi energy level of *n*- or *p*-doped organic semiconductors was statistically investigated based on the combination of classical semiconductor physics and energy distribution theory.^[56,57] It was argued that the process of molecular doping in organic semiconductors, be it through integer charge transfer or orbital hybridization, must be regarded as a modification of the density of states in the organic semiconductor upon dopant admixture and the Fermi-Dirac occupation at a certain temperature determines the doping efficiency.^[58]

No matter which model we can apply on doping process in organic semiconductors, charge generation needs to be analyzed in terms of two processes, namely, CTC (or ion pair) formation between host and dopant molecules (ionized dopant-host pair for integer charge transfer model and hybrid charge transfer complex for orbital hybridization model, hereafter

represented by CTC for the both pairs), and dissociation of free carriers from CTCs. Therefore, the charge generation efficiency can be expressed by

$$\eta_{CG} = \frac{N_{CTC}}{N_{dopant}} \times \frac{N_{free-carrier}}{N_{CTC}} = \eta_{CTC} \times \eta_{disso} \quad (2.1)$$

where η_{CG} is the charge generation efficiency, and N_{dopant} , N_{CTC} , and $N_{free-carrier}$ are the number densities of the dopant molecules, CTCs, and free charge carriers, respectively. η_{CTC} and η_{disso} are the formation and dissociation efficiencies of the CTC, respectively. The behavior of these two efficiencies should be investigated separately in order to establish quantitative description of doping characteristics. While change of electrical properties upon doping has been reported in many studies,^[11,12,14,17,55,59–68] there are few results relating the charge generation process itself to the CTC formation and dissociation up to now.^[13,15,56,69] Recently, η_{CTC} of a p-doped organic semiconductor was measured to be in the range of 13–77% as determined by UV-Vis or FT-IR spectroscopy.^[15,69] In case of η_{disso} , no quantitative analyses on the dependence of η_{disso} on the doping concentration were reported to our best knowledge because it is hard to consider the dopant aggregation or the charge trapping effect. Furthermore, there are few results for n-doped organic semiconductors related to the charge generation process available to facilitate a comprehensive understanding of the doping phenomena due to their instability in the presence of air.^[70–75]

In this study, we comprehensively investigate charge generation process of n-doped organic semiconductors using Rb_2CO_3 -doped 2,2,2-(1,3,5-benzinetriyl)-tris(1-phenyl-1-H-benzimidazole) (TPBi). We measure η_{CTC} at various doping concentrations from the change in the UV-Vis-NIR absorption spectra of the host molecules upon doping. η_{CTC} linearly decreases from 82.8% to 47.0% as the doping concentration (C) increases from 2.5 mol% to 20 mol%. The equation of CTC formation efficiency including constant of dopant aggregation is firstly introduced to quantitatively characterize aggregation property of dopant. η_{disso} calculated with η_{CTC} and carrier density decreases from 3.4% to 1.6%. The change of dissociation efficiency with doping concentration is interpreted in view of the classical semiconductor model and the orbital hybridization model.

2.2 Experimental methods

We investigate a doped organic semiconductor consisting of 1,3,5-Tri(1-phenyl-1H-benzo[d]imidazol-2-yl)phenyl (TPBi) (Nichem Co. Ltd.) as the host molecule and Rb_2CO_3 (Sigma-Aldrich Co. LLC.) as the dopant molecule. All doped thin films are fabricated by co-evaporating TPBi and Rb_2CO_3 molecules at room temperature. Samples are encapsulated with moisture getter in the dry nitrogen glove box prior to the measurement. The absorption spectra are measured using the Cary 5000 UV-Vis-NIR spectrophotometer and calibrated

XPS measurements are performed using a hemispherical electron energy analyzer. Since the analysis chamber is directly connected to the evaporation chamber, thermally deposited Rb_2CO_3 thin film is characterized without breaking the vacuum condition. The XPS core level scan is performed by $\text{Mg K}\alpha$ ($\hbar\omega = 1253.6 \text{ eV}$) photon lines. Using Alq_3 thin film, which is thermally stable compounds, and Rb_2CO_3 powder, the different cross sections of C $1s$, O $1s$ and Rb $3d$ core level peaks is considered for the quantitative analysis. For Rb $3d$ core level spectra, the reference value of spin-orbit splitting energy (1.49 eV) and intensity ratio for spin-orbit split two peaks (3:2) is considered as a fitting parameter. All spectra are fitted based on a Shirley-background correction.

The device structure of metal-insulator-semiconductor (MIS) devices is ITO (150 nm)/LiF (150 nm)/ Rb_2CO_3 -doped TPBi (200 nm)/ Rb_2CO_3 (1 nm)/Al (100 nm). Before evaporation, ITO is cleaned using acetone and isopropyl alcohol. Impedance analysis is carried out by a 1260 impedance/gain-phase analyzer and a 1287 electrochemical interface (Solartron). Considering the capacitance loss spectrum, the AC frequency is determined to be 200 Hz and the amplitude is 50 mV.

2.3 Charge transfer complex formation efficiency

Rb_2CO_3 doped TPBi films are thermally evaporated onto a glass substrate and encapsulated in a glove box immediately after deposition. The number of TPBi molecules in all samples is monitored by the quartz crystal monitor and is fixed

as that of the 50 nm thick TPBi pristine film. Figure 2.1(a) shows the UV-Vis-NIR absorption spectra of Rb_2CO_3 -doped TPBi thin films. As doping concentration increases, the peak intensity of intrinsic TPBi (304 nm) is reduced and those of CTC (479 and 600 nm) are increased. The change in the absorption spectra indicates CTC formation between the TPBi and Rb_2CO_3 molecules. Since absorbance is linearly dependent on the concentration of molecules according to the Beer-Lambert law, we can calculate the reduced number of neutral TPBi molecules, i.e. the number of CTCs, from the peak intensity of neutral TPBi at 304 nm. To remove the reflected light loss from the surface of the analyzed film, we calibrated the absorption spectra of all samples by subtracting the calculated reflection using the transfer matrix method with the refractive indices (n , k) of the TPBi film measured by variable angle spectroscopic ellipsometry. Figure 2.1(b) represents the UV-Vis-NIR absorption spectra after the calibration. The CTC formation efficiency (η_{CTC}), i.e., the ratio of the number density of CTCs (N_{CTC}) to dopant molecules (N_{dopant}), can then be derived according to following

$$\eta_{CTC} = \frac{N_{CTC}}{N_{dopant}} = \frac{100-C}{C} \times \frac{N_{CTC}}{N_{host}} \quad (2.2)$$

where C and N_{host} are the doping concentration (mol%) and the number density of the host molecules, respectively. N_{CTC}/N_{host} can be obtained by the relative ratio of the reduced peak intensity of neutral TPBi. The CTC

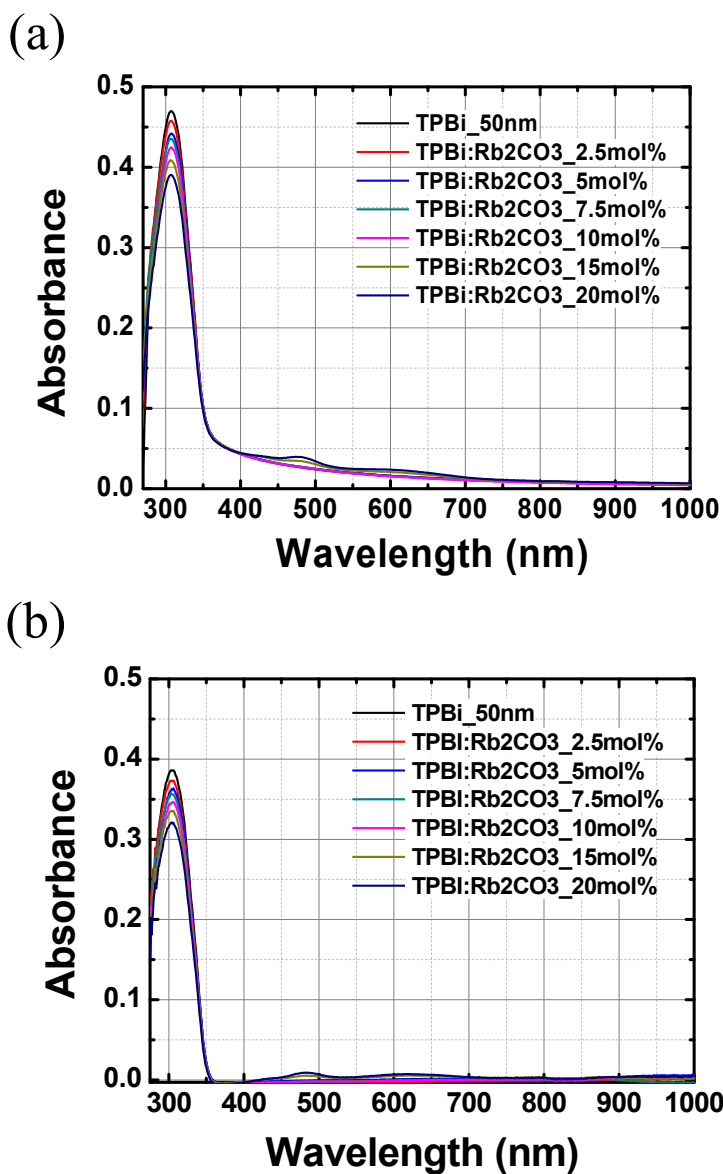


Figure 2.1 (a) UV-Vis-NIR absorption spectra of Rb_2CO_3 -doped TPBi thin film, and (b) calibrated absorption spectra without reflection. The number of TPBi molecules in all sample is fixed as that of the 50 nm TPBi pristine thin film.

formation efficiency obtained from this method is displayed in Figure 2.2. The CTC formation efficiency linearly decreases from 82.8% to 47.0% as the doping concentration increases from 2.5 mol% to 20 mol%. We consider that a decrease in η_{CTC} originates from the aggregation of dopant molecules, assuming all encounters between host and dopant molecules lead to the formation of CTCs.^[14,55] In order to analyze aggregation property quantitatively, degree of reduced CTC formation, δ_{CTC} , is introduced and defined by eq 2.3. From mathematical derivation of the definition, doping concentration-dependent η_{CTC} and δ_{CTC} can be expressed by

$$\delta_{CTC} = \frac{N_{CTC}^0 - N_{CTC}}{N_{CTC}^0} = f(N_{dopant}) \quad (0 \leq \delta_{CTC} \leq 1) \quad (2.3)$$

$$\eta_{CTC} = \eta_0 - \eta_0 \delta_{CTC} \quad (N_{dopant} > 0) \quad (2.4)$$

where η_0 and N_{CTC}^0 are the values of η_{CTC} and N_{CTC} at the situation where all dopants are surrounded by host molecules. Degree of reduced CTC formation is defined as ratio between the reduced number of CTCs due to aggregation and the number of CTCs at extreme dilution. By the definition, degree of dopant aggregation is dependent on dopant concentration and has the value between 0 and 1. If aggregation property of dopant is strong, degree of reduced CTC formation will have high value. From experimental result, a linear decrease of CTC formation efficiency with doping concentration indicates that degree of reduced CTC formation is linearly proportional to doping

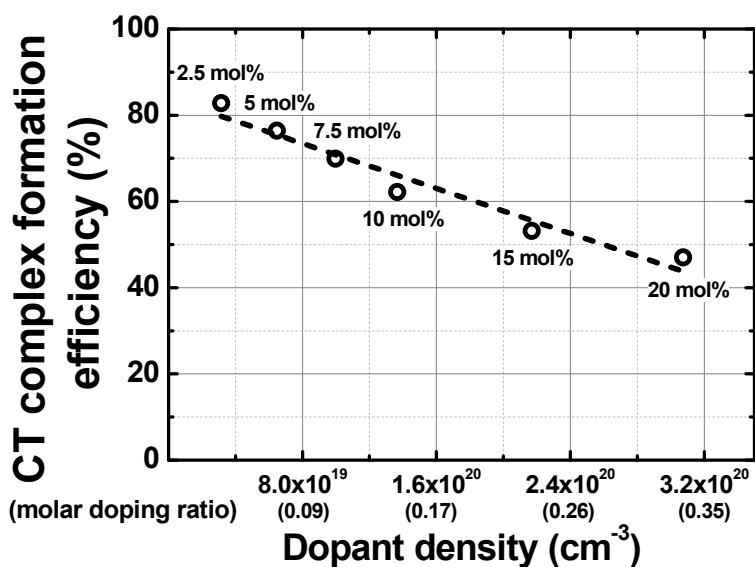


Figure 2.2 CTC formation efficiency of Rb_2CO_3 -doped TPBi thin film with various dopant densities. Dashed line is the linear fit of the data. CTC formation efficiency is the ratio of the number density of CTCs to dopant molecules. The linear decrease of CTC formation efficiency means that both the number and the size of aggregates increase simultaneously.

concentration. δ_{CTC} of Rb_2CO_3 increases from 0.17 to 0.53. It means that at high doping concentration the half number of CTCs is formed due to aggregation. With the equation of CTC formation efficiency, characteristics of dopant aggregation can be described. In the extreme case where δ_{CTC} is constant and η_0 is 100%, aggregation of dopants will not occur. If δ_{CTC} is constant and η_0 is lower than 100%, only the number of aggregated dopant cluster would increase with fixed average size as the doping concentration is increased. The linear decrease of CTC formation efficiency with increasing doping concentration of Rb_2CO_3 and lower η_0 than 100% in our results indicate that both the number and the size of aggregates increase simultaneously. In this case, if each cluster is able to transfer one electron, the average number of dopant molecules per cluster would increase from 1.21 at 2.5 mol% to 2.13 at 20 mol%. The number density of CTCs increases from 1.54×10^{19} to $1.42 \times 10^{20} \text{ cm}^{-3}$. Introduction of the equation will facilitate quantitative comparison of aggregation property of various dopants. Future work will include detailed investigation of aggregation property for various dopants using behavior of CTC formation efficiency. This analysis of CTC formation efficiency is based on in situ X-ray photoemission spectroscopy (XPS) results that show 1.34 effective dopants are produced per Rb_2CO_3 molecule during thermal deposition, as described below.

2.4 Decomposition of Rb₂CO₃ based on in situ XPS

measurements

The decomposition of alkali metal compounds during the thermal evaporation was reported using in situ XPS.^[76–78] Accordingly, the thermal decomposition of Rb₂CO₃ is investigated by in situ XPS. Figure 2.3 shows the XPS core level spectra of (a) Rb 3*d* and (b) O 1*s* (c) C 1*s* for Rb₂CO₃ film deposited on an Au substrate. The Au substrate is cleaned by Ar⁺ sputtering before deposition. In the region of the C 1*s* core level, the spectrum fitted with Voigt functions is composed of three distinct bonding features that have binding energy peaks at 286.1, 287.3, and 290.3 eV, respectively. These carbon peaks do not result from contamination of the deposition chamber because carbon peaks are not observed when intrinsic Rb is deposited. The Rb₂CO₃ molecule has only one bonding feature corresponding to a carbon of carbonate, CO₃²⁻, and represents the binding energy of ~290 eV.^[79] Thus, the three binding energy peaks suggest that evaporated Rb₂CO₃ would have at least three kinds of carbon bonding, including the carbonate bond. Considering these characteristics, we can speculate on the thermal deposition process of Rb₂CO₃ as follows. First of all, Rb₂CO₃ decomposes into Rb, O₂, and CO₂ when the temperature is raised.



These gas components could be the reason for the increasing base pressure in the vacuum chamber during thermal evaporation. Thereafter, O₂ and CO₂ gas

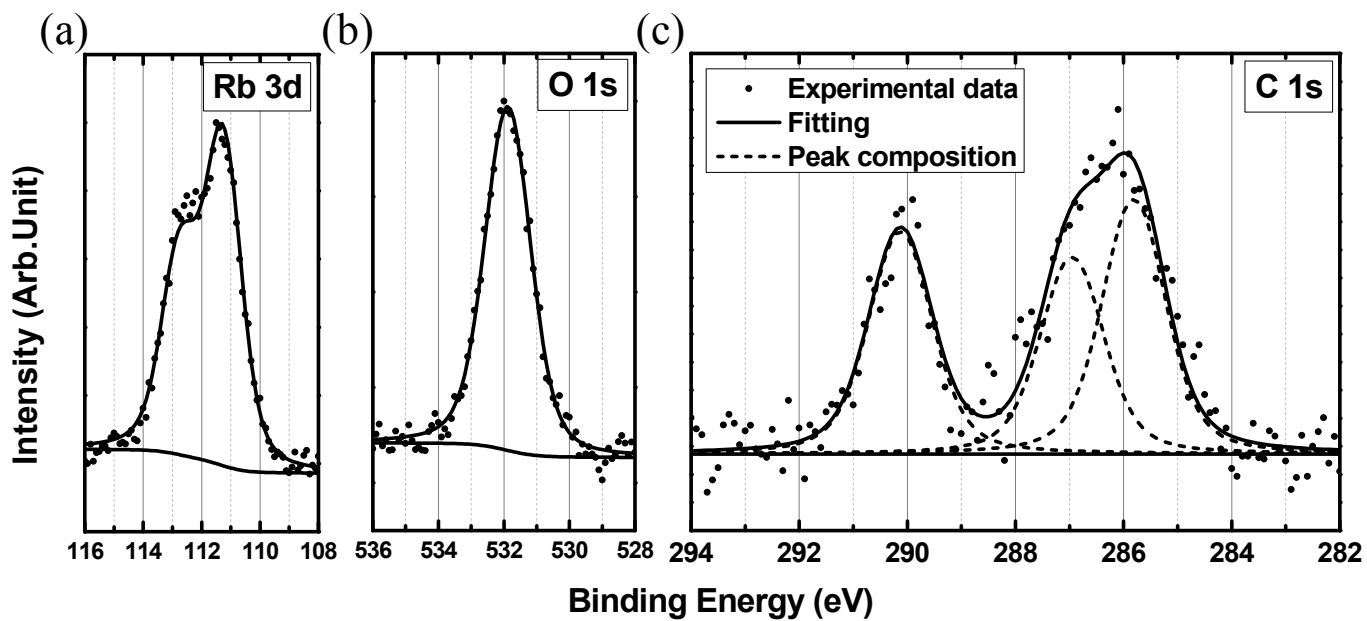
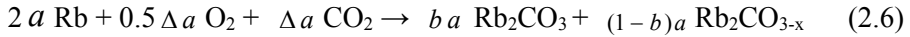


Figure 2.3 (In situ) XPS core level spectra of (a) Rb 3*d* (b) O 1*s* and (c) C 1*s* for evaporated Rb₂CO₃ film on Au substrate. The decomposed peaks represent the results of peak fitting with Voigt functions.

in the vacuum chamber react with Rb again in the process of deposition, and Rb_2CO_3 and $\text{Rb}_2\text{CO}_{3-x}$ are produced by following reaction.



a is introduced in the purpose of calculating amount of reacted Rb and b means relative ratio between Rb_2CO_3 and $\text{Rb}_2\text{CO}_{3-x}$. Δa means non-perfect stoichiometry of the reaction. Therefore, the peak at 290 eV originates from Rb_2CO_3 ^[79] and other peaks can be attributed to $\text{Rb}_2\text{CO}_{3-x}$. The relative area ratio of the Rb 3*d* peak with respect to the C 1*s* peak of carbonate (290 eV) must be kept in the ratio of 2:1 when a Rb_2CO_3 molecule is deposited without thermal decomposition during the deposition. In our measurements, however, the ratio is shown to be 3.03:1. To determine the effective dopant density, we quantitatively calculate the amount of Rb, Rb_2CO_3 , and $\text{Rb}_2\text{CO}_{3-x}$ from the relative area ratio between each Rb 3*d* and C 1*s* peak of 290 eV and others. Based on this analysis, 0.68, 0.22, and 0.44 of Rb, Rb_2CO_3 , and $\text{Rb}_2\text{CO}_{3-x}$ molecules are produced per 1 Rb_2CO_3 molecule, respectively. Since the oxygen states in Rb_2CO_3 and $\text{Rb}_2\text{CO}_{3-x}$ in the O 1*s* spectra is not clearly resolved within instrumental resolution (~ 1 eV), O 1*s* spectra is not considered for quantitative analysis. Assuming that each molecule (i.e. Rb, Rb_2CO_3 , and $\text{Rb}_2\text{CO}_{3-x}$) can take part in the doping process, we use N_{dopant} as the effective dopant density as with 1.34 effective dopants per Rb_2CO_3 molecule. The CTC formation efficiency is obtained from the effective dopant density.

2.5 Charge generation efficiency and dissociation efficiency

The CTC formation efficiency of Rb_2CO_3 -doped TPBi is higher than the charge generation efficiency for all doping concentrations. In their recent paper, Pingel et al. analyzed the UV-Vis absorption spectra of fully ionized P3HT and F4-TCNQ molecules to determine the fraction of ionized molecules.^[15] From these results and our experimental data, it is shown that the formation of CTCs from dopant and host molecules is not the limiting process of molecular doping in organic semiconductors when the energy level difference between the HOMO (for p-type doping) or LUMO (for n-type doping) of a host and Fermi level of dopant is sufficient. To determine the dissociation efficiency, we fabricated metal-insulator-semiconductor (MIS) devices to measure the charge carrier density.^[11,12,80] The device structure is ITO (150 nm)/LiF (150 nm)/ Rb_2CO_3 -doped TPBi (200 nm)/ Rb_2CO_3 (1 nm)/Al (100 nm). The intrinsic Rb_2CO_3 layer is used for efficient electron injection to equalize the electron injection barrier in all devices. The AC frequency of impedance spectroscopy is 200 Hz as determined from the loss spectrum (G/ω), and the amplitude is 50 mV. We obtain the charge carrier density using Mott-Schottky equation

$$N_{\text{free-carrier}} = \frac{2}{q\epsilon_0\epsilon_r} \frac{\partial C_p^{-2}}{\partial V} \quad (2.7)$$

where q , ϵ_0 , ϵ_r , C_p , and V are the elementary charge, vacuum permittivity, dielectric permittivity, capacitance, and DC voltage, respectively. The Mott-

Schottky plot and loss spectrum of the MIS devices are displayed in Figure 2.4. In Figure 2.5, the carrier density of Rb₂CO₃-doped TPBi linearly increases from 8.9×10^{17} to $2.2 \times 10^{18} \text{ cm}^{-3}$ with increasing doping concentration. Linearity between the carrier density and the doping concentration is reported in many doped systems.^[11,12,80,81] Accordingly, carrier density can be expressed by following

$$N_{free-carrier} = sN_{dopant} + n_0 \quad (2.8)$$

where s and n_0 are the slope of the change in carrier density and the intercept, respectively. At this point, the equation describes the change of carrier density in the range of a few mol%. Therefore, there is the lack of correspondence between n_0 and intrinsic carrier density. The values of s and n_0 are 4.47×10^{-3} and $8.74 \times 10^{17} \text{ cm}^{-3}$. The charge generation efficiency and dissociation efficiency can finally be expressed from the linearity of the CTC formation efficiency and the carrier density with increasing doping concentration as follows

$$\eta_{CG} = \frac{N_{free-carrier}}{N_{dopant}} = \left(\frac{n_0}{N_{dopant}} + s \right) \quad (2.9)$$

$$\eta_{disso} = \frac{N_{free-carrier}}{N_{CTC}} = \frac{sN_{dopant} + n_0}{-\delta_{CTC}N_{dopant} + \eta_0 N_{dopant}} \quad (2.10)$$

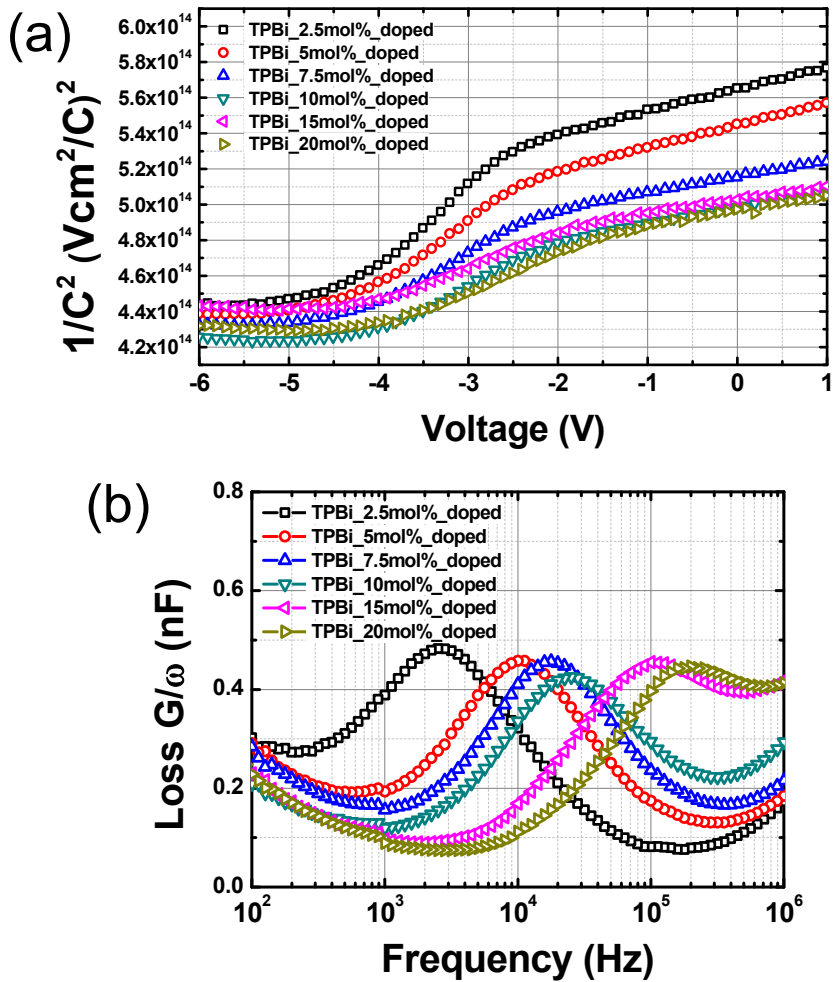


Figure 2.4 (a) Capacitance-voltage characteristics of MIS (metal-insulator-semiconductor) devices at various doping concentrations. (b) Capacitance loss spectrum (G/ω) of MIS devices.

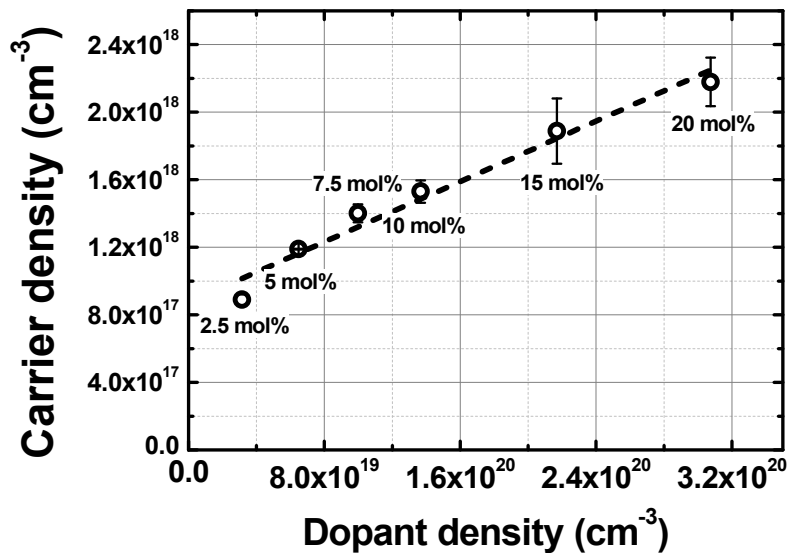


Figure 2.5 Charge carrier density of Rb_2CO_3 -doped TPBi layer from Mott-Schottky analysis. The device structure is ITO (150 nm)/LiF (150 nm)/ Rb_2CO_3 -doped TPBi (200 nm)/ Rb_2CO_3 (1 nm)/Al (100 nm). Dashed line is the linear fit of the data ($N_{\text{free-carrier}} = sN_{\text{dopant}} + n_0$).

The charge generation efficiency and dissociation efficiency are depicted in Figure 2.6(a). In the low doping concentration regime ($N_{\text{dopant}} < 2 \times 10^{20} \text{ cm}^{-3}$), the charge generation efficiency and dissociation efficiency decreased substantially with doping concentration. The dissociation efficiency saturates to 1.6% in the high doping concentration regime ($N_{\text{dopant}} > 2 \times 10^{20} \text{ cm}^{-3}$). This concentration-dependent dissociation behavior can be described by activation from the donor level according to the classical semiconductor theory.^[82]

$$N_{\text{free-carrier}} \approx N_D^+ = \frac{N_{\text{Dopant}}}{1 + \exp[(E_F - E_D) / k_B T]} \quad (2.11)$$

N_D^+ , E_F , E_D , k_B and T are the number density of ionized dopant, the Fermi level, the donor level, the Boltzmann constant and temperature, respectively. In this equation, N_{dopant} can be substituted by N_{CTC} since N_{CTC} is the actual number density of dopant considering dopant aggregation. Using the equation, the doping concentration-dependent energy difference between the Fermi level and the donor level can be obtained from the dissociation efficiency. The change of the position of the Fermi level relative to the donor level is displayed in Figure 2.6(b). The Fermi level shifts from 86.5 meV at $3.15 \times 10^{19} \text{ cm}^{-3}$ to 106.1 meV at $3.07 \times 10^{20} \text{ cm}^{-3}$ above the donor level as the doping concentration increases. The shift of the Fermi level away from the donor level toward LUMO level with increasing dopant density can be understood from the increased electron density with increasing doping concentration leading to lower activation probability of dopant. Similar

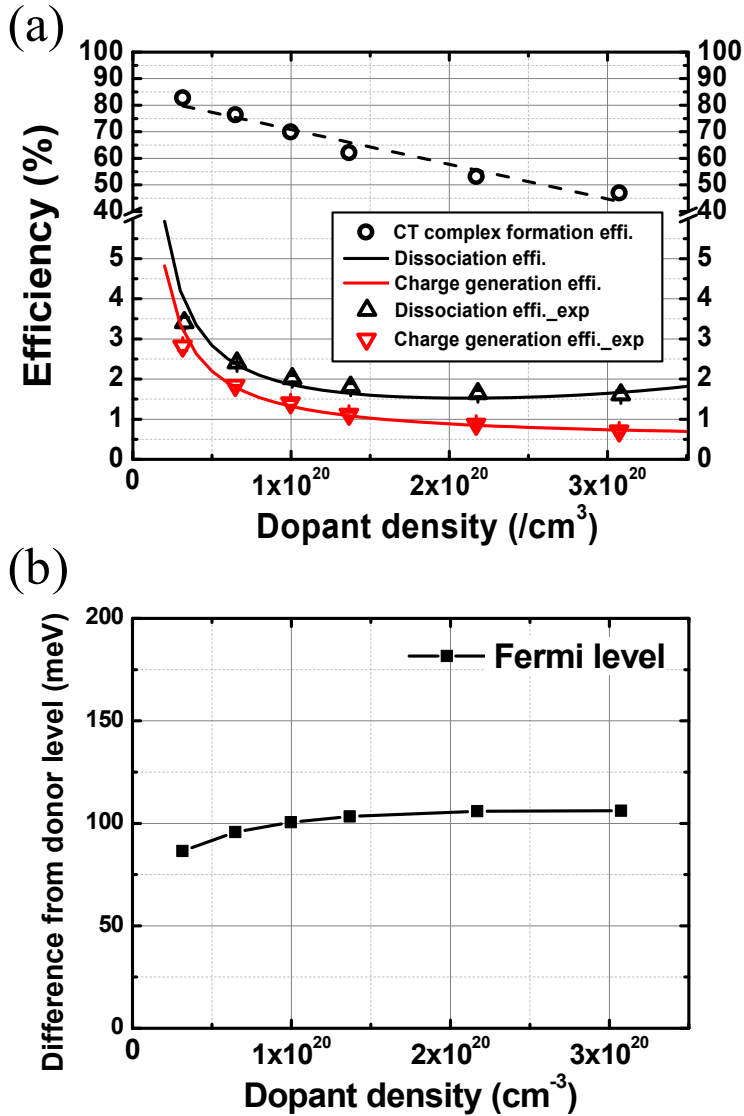


Figure 2.6 (a) Formation and dissociation efficiencies of CTC. Dotted data are obtained from the experiment. Dashed line is the fitted line of CTC formation efficiency and the solid lines represent the calculated dissociation efficiency and charge generation efficiency using the constant derived from experimental data. (b) Energetic position of Fermi level relative to donor level based on Fermi-Dirac distribution of single donor level.

discussion can be applied to the orbital hybridization model. According to the model, frontier orbital hybridization between host and dopant results in formation of hybrid charge transfer complex whose HOMO level is located below LUMO level of host. Since the Fermi level increases with increasing doping concentration, ionization probability of the CTC to the LUMO of host will be reduced again upon increasing doping concentration.

2.6 Conclusion

We investigate the charge generation efficiency in terms of CTC formation efficiency and dissociation efficiency of Rb_2CO_3 -doped TPBi thin film. Analysis of peak intensities in the TPBi UV-Vis-NIR spectra can lead to quantitative derivation of the CTC formation efficiency, which linearly decreases as the doping concentration increases. For the first time the quantitative method for characterizing aggregation property is introduced. Given that the slope of the curve of CTC formation efficiency against doping concentration is negative in our experimental results, it is shown that both the number and size of dopant aggregation increase simultaneously. Moreover, degree of reduced CTC formation as a function of doping concentration is introduced. The degree of reduced CTC formation will provide an intuitive perspective of effectiveness of dopants in various doping concentration. Low charge generation efficiency (2.8%) compared to the high CTC formation efficiency (82.8%) indicates that the dissociation of bounded charge from the

charge transfer complex is the most impeding process in the electrical doping of organic semiconductors. The doping concentration-dependent behavior of dissociation efficiency is firstly analyzed experimentally. The dissociation efficiency decreases from 3.4% at $3.15 \times 10^{19} \text{ cm}^{-3}$ to 1.6% at $3.07 \times 10^{20} \text{ cm}^{-3}$. The reduction of dissociation efficiency with increasing doping concentration can be explained by the reduced ionization probability originating from the shift of the Fermi level located above donor level away from the donor level (CTC HOMO level in the orbital hybridization model) due to the increased electron density with increasing doping concentration. This study contributes to further understanding the charge generation process of doping in organic semiconductors. In the future, doping technology based on established principle and theory will make precise parameter control and efficient doping process feasible for organic electronics such as organic light-emitting diodes, organic photovoltaic devices, and organic thin-film transistors.

Chapter 3. Mobility Balance in the Light-emitting Layer Governs the Polaron Accumulation and Operational Stability of Organic Light-Emitting Diodes

3.1 Introduction

The efficiency of organic light-emitting diodes (OLEDs) has been significantly improved by harvesting triplet excitons using phosphorescence or thermally-activated delayed fluorescence (TADF).^[83–85] Concurrently, the electro-optical properties of OLEDs are well-understood in terms of their optics, photo-physics, and electrical theory. Highly efficient OLEDs displaying high external quantum efficiencies (> 30%) have been reported.^[86–94] The theoretical maximum efficiency of OLEDs has been estimated from modeling and realized experimentally.^[95–98] However, although much research has focused on the operational stability of OLEDs, the degradation mechanism of OLEDs has not yet been fully elucidated.^[24,26,27,99–103] Recently, Zhang et al. demonstrated a 10-fold enhancement in device lifetime with blue phosphorescent OLEDs.^[104] They observed that gradually changing the doping concentration of the emitting dopant from the emitting layer (EML) to the hole transporting layer (HTL) reduced the exciton density due to a broadened recombination zone. Because of the low exciton density, exciton–polaron annihilation, which is considered as one of the main sources of material degradation, was suppressed, resulting

in a longer device lifetime. In the same context, Wang et al. reported that interactions between excitons and polarons play a crucial role in material decomposition and dopant aggregation.^[105–107] The encounter of optically formed singlet excitons and accumulated polarons between the organic layers dramatically increases the driving voltage of hole-only devices. Enhancement of operational stability via controlling the recombination zone,^[104,108,109] charge injection,^[110] and exciton quencher^[111,112] has been examined to reduce exciton–polaron interactions. These reports indicate that control of polarons and excitons is important for the design of a stable device. In this paper, we report that minimizing polaron accumulation in the EML is an important physical factor for enhancing the lifetime of an OLED device; the electrochemical stability of the materials remains important. Parallel capacitance–voltage characteristics allow the charge dynamics of OLEDs consisting of a single host and exciplex-forming co-host to be understood and correlated with operational lifetimes, in turn determined by impedance spectroscopy and drift-diffusion simulations. The results indicate that the balance between electron and hole mobilities in the EMLs significantly affects exciton and polaron density distributions in the devices. The lifetime of an exciplex-forming co-host-based device, in which the accumulated polaron density is lower than that in a single host-based device, is double that of the single host-based device, and this can be achieved without lowering the efficiency. This indicates that understanding the charge dynamics of OLEDs is another route to enhancing operational stability.

3.2 Experimental methods

Organic materials were vacuum-deposited on ITO-coated glass substrates at a pressure of 5×10^{-8} Torr. All devices were characterized after encapsulation with a moisture-getter in a glovebox. The J–V–L characteristics were measured using Keithley 2400 and Photo Research PR650 spectrometers. The EQEs were obtained considering both normal luminance and angle-dependent electroluminescence using Keithley 2400 and Ocean Optics S2000 spectrometers. The operational lifetime of a device was measured using the Polaronix M6000T lifetime measurement system under the constant current condition corresponding to $1,000 \text{ cd m}^{-2}$. Capacitance–voltage characteristics were measured using a Solartron 1260 impedance/gain-phase analyzer with a Solartron 1287 potentiostat.

3.3 Structure design and performance of OLEDs

Figure 3.1(a) shows the EML structures of the OLEDs used in this study. Device 1 was an exciplex-forming co-host-based OLED and device 2 was a single host-based OLED. 3,3-di(9H-carbazol-9-yl)biphenyl (mCBP) and 9,10-bis(3-(pyridin-3-yl)phenyl)anthracene (DPyPA) were used as the HTL and electron transporting layer (ETL), respectively.^[113] As an exciplex-forming co-host in device 1, mCBP and 3',3''',3''''-(1,3,5-triazine-2,4,6-triyl)tris((1,1'-biphenyl)-3-carbonitrile) (CN-T2T) were selected as donor and acceptor hosts, respectively.^[114] (4s,6s)-2,4,5,6-tetra(9H-carbazol-9-yl)isophthalonitrile

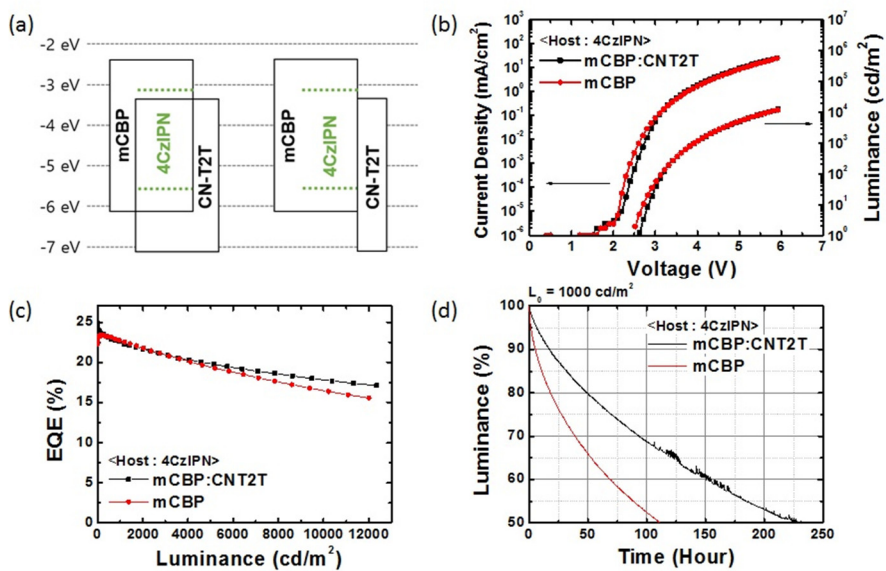


Figure 3.1 (a) Emitting layer (EML) structures, (b) current density–voltage–luminance (J–V–L) results, (c) external quantum efficiency–luminance (EQE–L) data, and (d) operational lifetimes of exciplex-forming host and single host-based OLEDs. Device lifetimes were measured under the constant current condition at the initial luminance of 1,000 cd m⁻².

(4CzIPN) was used as the light-emitting dopant via the TADF mechanism.^[115] In device 2, the CN-T2T was located between the EML and ETL to simultaneously form an interface exciplex with mCBP and block triplets from the EML. The complete device structure was indium tin oxide (ITO) (70 nm)/mCBP:MoO₃ (45 nm)/mCBP (20 nm)/EML (30 nm)/CN-T2T (10 nm)/DPyPA (45 nm)/Rb₂CO₃ (1 nm)/Al (100 nm). All of the materials used in devices 1 and 2 were identical to eliminate the effect of changes in materials on device stability. It was reported that a 15 wt% doping concentration of 4CzIPN in the mCBP host provided the longest device lifetime;^[29] the doping concentration of 4CzIPN in device 2 was accordingly set at 15 wt%. For device 1, the doping concentration of 4CzIPN was 5 wt%, to induce mobility balance by increasing the proportion of co-hosts.^[97]

Bond dissociation energies (BDEs) are an indication of chemical stability. The BDEs of the charge transporting materials were calculated using the Jaguar quantum chemical calculation code^[116,117] in the Schrödinger Materials Science Suite;^[118] the results are listed in Table 3.1. In the neutral state, the BDEs of all of the materials in the neutral state exceed 3 eV. However, the BDE of the anionic state of mCBP is 1.83 eV, which indicates that the negative polaron state of mCBP is unstable compared with other states. Similarly, the BDE of the cationic state of CN-T2T containing an electron accepting moiety is 2.94 eV, which is smaller than the BDE of the anionic state. In contrast, DPyPA has BDEs higher than 4 eV for all of its states.

	mCBP	CN-T2T	DPyPA
Neutral	3.63	4.92	4.71
Anionic	1.83	3.79	4.04
Cationic	4.46	2.94	5.47

Table 3.1 Calculated bond dissociation energies (BDEs, units of eV) of materials used as charge transports and hosts in OLEDs

Figure 3.1(b) and (c) show the current density–voltage–luminance (J–V–L) and external quantum efficiency–luminance (EQE–L) characteristics of the OLEDs. The turn-on voltages were 2.6 and 2.5 V and the maximum EQEs were 24.9 and 23.4% for devices 1 and 2, respectively. The EQEs of devices 1 and 2 decreased with increasing luminance, to 17.7 and 16.4%, respectively, at 10,000 cd m^{-2} . The roll-off characteristics will be discussed along with the results of charge dynamics analysis later in this article. Figure 3.1(d) displays the lifetime of the devices. The device lifetime was measured under the constant current condition at an initial luminance of 1,000 cd m^{-2} . The LT50 lifetimes were 225 and 111 h for devices 1 and 2, respectively. Notably, the lifetime of device 1 was twice that of device 2, without a lower EQE even though the constituting materials were identical.

3.4 Understanding of charge behavior by impedance spectroscopy and drift-diffusion numerical modeling

The capacitance–voltage characteristics were measured using impedance spectroscopy to understand how the charge dynamics of the OLEDs correlated with operational stability.^{41–52} Figure 3.2(a) displays the capacitance–voltage characteristics of the devices, along with their luminance and current density characteristics. The dotted data are the experimental results and the solid lines represent the simulation results. The frequency and amplitude of the AC voltage were set at 500 Hz and 100 mV, respectively, because the capacitance

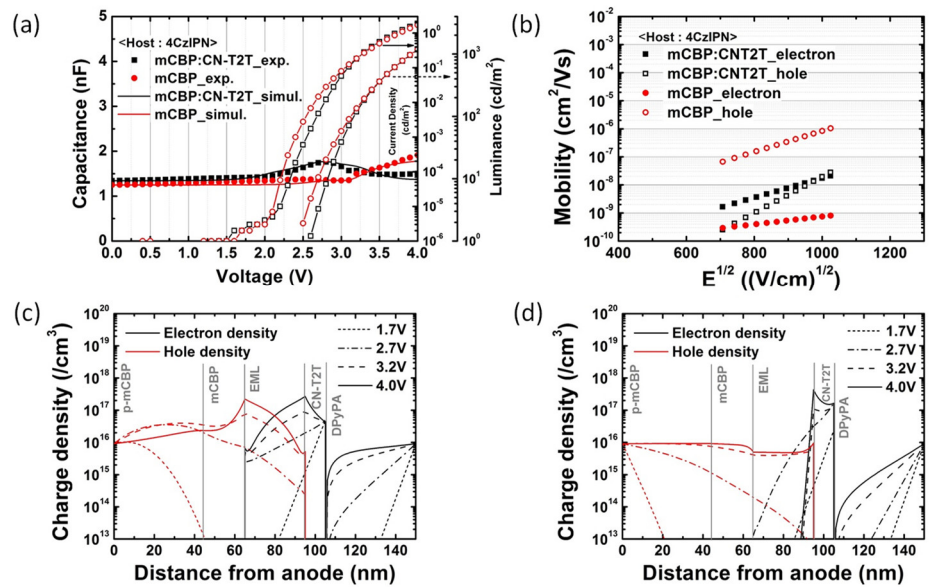


Figure 3.2 (a) Parallel capacitance–voltage characteristics of OLEDs as a function of luminance and current density. The dotted lines are experimental results and the dashed lines are calculated results from drift-diffusion numerical modeling. The frequency and amplitude of the AC voltage were 500 Hz and 100 mV, respectively. (b) Field-dependent electron and hole mobilities of the EMLs. The mobility was obtained by analyzing the space-charge limited current of charge-only devices. (c, d) The distribution of the local charge densities of electrons and holes at different voltages in (c) exciplex-forming and (d) single host-based OLEDs calculated by drift-diffusion simulations.

contribution due to trap response appeared at frequencies lower than 100 Hz.^[36,40] At 0 V, the capacitances were 1.34 and 1.25 nF for devices 1 and 2, respectively. In the absence of electrical bias, electrons and holes are not injected from the electrodes. Therefore, the values at 0 V are close to the geometrical capacitances because all organic layers of the devices act as dielectric plates between the electrodes. In device 1, the capacitance slightly increased with increasing voltage from 1.34 nF at 0 V to 1.43 nF at 2 V. A further increase in the voltage increased the capacitance and the devices began to emit light. The capacitance reached 1.76 nF at 2.8 V, decreased to 1.48 nF at 3.2 V, and then remained constant at higher voltages. Device 2 showed different behavior. Its capacitance slightly increased from 1.25 nF at 0 V to 1.37 nF at 2.6 V, and then increased continuously from 1.35 nF at 3.1 V to 1.90 nF at 4 V. This indicated that polarons were accumulating in the device with increasing voltage. Drift-diffusion modeling was performed to further understand the relationship between device lifetime and capacitance–voltage characteristics.⁵³ The charge carrier mobilities of the materials were measured from the space-charge-limited current of single carrier devices depicted in Figure 3.3. Figure 3.2(b) shows the electron and hole mobilities of the exciplex-forming co-host-based EML and the single host-based EML. The device structures of the single carrier devices were ITO (70 nm)/ReO₃ (1 nm)/EML (100 nm)/ReO₃ (1 nm)/Al (100 nm) and ITO (70 nm)/Rb₂CO₃ (1 nm)/EML (100 nm)/Rb₂CO₃ (1 nm)/Al (100 nm) for holes and electrons, respectively. The electron and hole mobilities of the EML in device 1 were 1.75×10^{-8} and 1.96×10^{-8} cm² V⁻¹ s⁻¹, respectively,

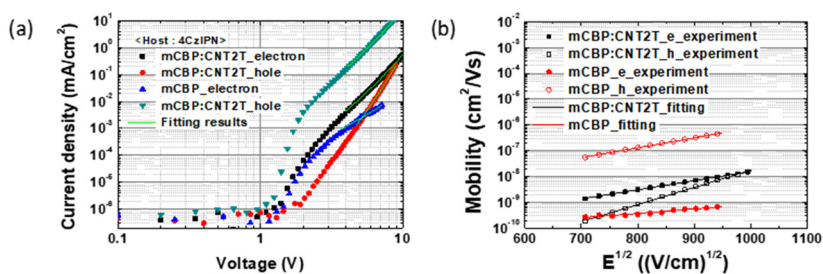


Figure 3.3 (a) Current density–voltage characteristics of single carrier devices consisting of an exciplex-forming co-host based emitting layer (EML) and a single host-based EML. (b) Experimental and fitted results of electron and hole mobilities under the application of space-charge limited current. The device structures of the hole- and electron-only devices were indium tin oxide (ITO; 70 nm)/ReO₃ (1 nm)/EML (100 nm)/ReO₃ (1 nm)/Al (100 nm) and ITO (70 nm)/Rb₂CO₃ (1 nm)/EML (100nm)/Rb₂CO₃ (1 nm)/Al (100 nm), respectively.

at an electric field strength of 10^6 V cm^{-1} . The corresponding values for the EML in device 2 were 7.45×10^{-10} and $8.42 \times 10^{-7} \text{ cm}^2 \text{ V}^{-1} \text{ s}^{-1}$. The mobility balance between two systems can be quantitatively compared using the mobility ratio, as follows:

$$\gamma_{\text{mobility}} = \begin{cases} \frac{\mu_{\text{hole}}}{\mu_{\text{electron}}} (\mu_{\text{electron}} < \mu_{\text{hole}}) \\ \frac{\mu_{\text{electron}}}{\mu_{\text{hole}}} (\mu_{\text{electron}} > \mu_{\text{hole}}) \end{cases} \quad (1 \leq \gamma_{\text{mobility}}) \quad (3.1)$$

where γ_{mobility} , μ_{electron} , and μ_{hole} are the mobility ratio, electron mobility, and hole mobility, respectively. By definition, the mobility ratio is equal to or larger than unity. At the electric field strength of 10^6 V cm^{-1} , the mobility ratios of the two EMLs were 1.1 and 1,136.4 for devices 1 and 2, respectively. The relatively balanced charge mobility of the exciplex-forming co-host-based EML was attributed to electron and hole transport that occurred mainly on the frontier orbitals of the donor and acceptor hosts. However, in a single host-based EML, electrons transport by hopping between the lowest unoccupied molecular orbital (LUMO) of the dopants because the LUMO of mCBP is very high (-2.4 eV). Meanwhile, holes can simultaneously transport through the highest occupied molecular orbital (HOMO) of mCBP and the dopants, which leads to about a 1,000-times lower electron mobility compared with the hole mobility. In the drift-diffusion numerical simulation, the charge transport in the semiconductor is described by a drift and diffusion mechanism. Poisson's

equation and the continuity relationship are given by:

$$\frac{\varepsilon_0 \varepsilon_r}{q} \frac{\partial^2 \varphi(x,t)}{\partial x^2} = p(x,t) - n(x,t) + N_D - N_A + \sum \rho_t(x,t) \quad (3.2)$$

$$\frac{\partial p(x,t)}{\partial t} = \frac{1}{q} \frac{\partial}{\partial x} \left[-\frac{\mu_p kT}{q} \frac{\partial p(x,t)}{\partial x} - \mu_p p(x,t) E(x,t) \right] + R(x,t) \quad (3.3)$$

where ε_0 , ε_r , q , φ , p , n , N_D , N_A , ρ_t , E , and R are the vacuum permittivity, dielectric permittivity, electronic charge, electric potential, hole density, electron density, ionized donor density, ionized acceptor density, trap charge, electric field, and recombination term, respectively. The physical parameters used in the calculation are listed in Table 3.2. Because impedance spectroscopy applied a single sinusoidal AC voltage to the device, the time-dependent parameters were expressed by Equations (3.4), (3.5), and (3.6):

$$n(x,t) = n_0(x) + \tilde{n}(x) e^{i\omega t} \quad (3.4)$$

$$p(x,t) = p_0(x) + \tilde{p}(x) e^{i\omega t} \quad (3.5)$$

$$\varphi(x,t) = \varphi_0(x) + \tilde{\varphi}(x) e^{i\omega t} \quad (3.6)$$

where n_0 , p_0 , and φ_0 and \tilde{n} , \tilde{p} , and $\tilde{\varphi}$ to the DC and AC components, respectively. The impedance of a device is obtained by dividing the voltage by the current in complex form.⁵⁴⁻⁵⁶ The calculated parallel capacitances are shown as solid lines in Figure 3.2(a). The simulated

Parameter	Value
Dielectric constant, ϵ_r	3.5
Valence band density of states, N_v	$1 \times 10^{21} \text{ cm}^{-3}$
Conduction band density of states, N_c	$1 \times 10^{21} \text{ cm}^{-3}$
Hole mobility, μ_{hole} , of mCBP ^a	$4.2 \times 10^{-5} \text{ cm}^2 \text{ V}^{-1} \text{ s}^{-1}$
Electron mobility, $\mu_{electron}$, of CN-T2T	$6.1 \times 10^{-5} \text{ cm}^2 \text{ V}^{-1} \text{ s}^{-1}$
Electron mobility, $\mu_{electron}$, of DPyPA	$7.4 \times 10^{-5} \text{ cm}^2 \text{ V}^{-1} \text{ s}^{-1}$
Injection barrier, ϕ	0.3 eV
Recombination coefficient, r	$6.7 \times 10^{-14} \text{ cm}^3 \text{ s}^{-1}$ (D1)
Recombination coefficient, r	$1.8 \times 10^{-12} \text{ cm}^3 \text{ s}^{-1}$ (D2)
Number of emitting dopants, $N_{dopants}$	$7.9 \times 10^{19} \text{ cm}^{-3}$ (D1)
Number of emitting dopants, $N_{dopants}$	$9.8 \times 10^{19} \text{ cm}^{-3}$ (D2)

^aat the electric field strength of 10^6 V/cm .

Table 3.2 Physical parameters used in the drift-diffusion numerical simulations.

capacitances as a function of applied DC voltage fitted well with the experimental results. The local charge distribution in the device was investigated at different voltages to correlate the trend of the capacitance with the charge dynamics. Figure 3.2(c) displays the distributions of electrons and holes in the exciplex-forming host-based OLED (device 1) at different voltages. At 1.7 V, the electron and hole densities injected from the electrodes were less than 10^{16} cm^{-3} . The small change of capacitance in this voltage regime was attributed to small injected charges. With increasing voltage up to 2.7 V, electrons and holes accumulated near the interfaces between the EML and the transporting layers, because of the relatively low electron and hole mobilities of the EML compared with those of the transporting layers. Therefore, the accumulation of polarons near the EML contributed to the increased capacitance in the turn-on voltage regime. In the EML, electrons and holes were symmetrically distributed over the layer. The symmetric distribution of the charges resulted from a balanced charge mobility between electrons and holes. In contrast, very different charge distributions were obtained for the single host-based OLED (device 2) (Figure 3.2(d)). Holes transported toward the EML without accumulating at the interface between the HTL and the EML, because the hole mobility of the EML in device 2 was much greater than that of the EML in device 1. Up to 2.7 V, which was the voltage after recombination of electrons and holes, polaron accumulation did not occur in the devices. The relatively constant capacitance of device 2 in the turn-on voltage regime compared with device 1 can be understood according to this analysis.

Meanwhile, the 1,000-times higher hole mobility versus electron mobility led to the accumulation of electrons at the interface between the EML and the ETL because of substantial retardation of the electrons. Electrons continuously accumulated as the voltage increased to 4 V. Holes also accumulated at the ETL side in the EML after 3.2 V because the amount of electrons injected to the EML was low. Consequently, the capacitance of device 2 increased above 3.1 V.

3.5 Recombination zone depending on the mobility ratio

The distribution of the exciton generation rate, which is thought of as a recombination zone, of devices 1 and 2 at 4 V is presented in Figure 3.4(a). Device 1 showed a uniform exciton generation rate lower than $3 \times 10^{20} \text{ cm}^{-3} \text{ s}^{-1}$ over the EML because of the balance in transport between electrons and holes. In contrast, the distribution of the exciton generation rate for device 2 was on the ETL side. The exciton generation rate at the interface between the EML and ETL was $6.2 \times 10^{21} \text{ cm}^{-3} \text{ s}^{-1}$, which was 20-times higher than that of device 1, and decreased to $1.0 \times 10^{15} \text{ cm}^{-3} \text{ s}^{-1}$ toward the center of the EML. A high exciton generation rate and high electron density in the ETL side of the EML would result in an increased probability of exciton and polaron encounters, which would lead to exciton-exciton and exciton-polaron quenching-induced degradation. As indirect evidence of exciton- and polaron-induced quenching, the EQE roll-off of device 2 was greater than that of device 1 (Figure 3.1(c)).

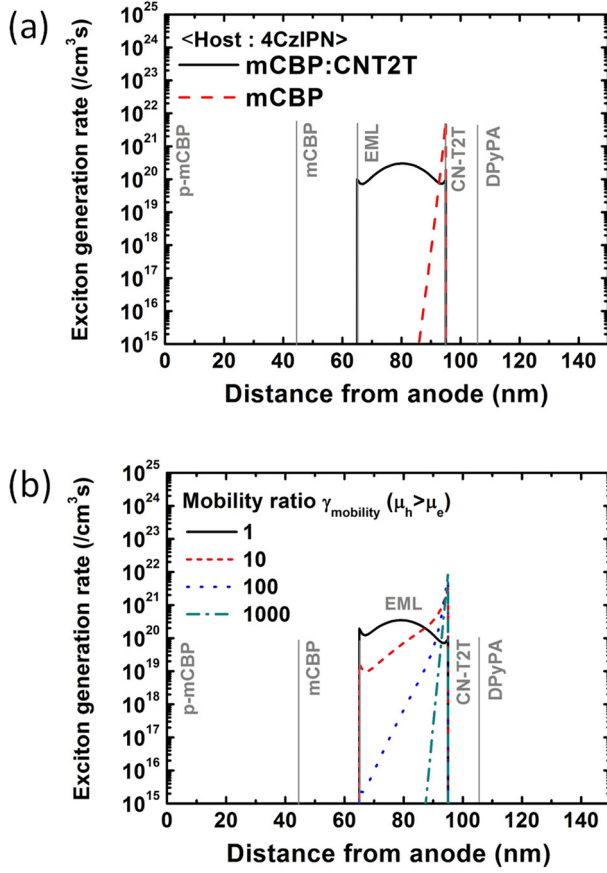


Figure 3.4 (a) Calculated local distributions of the exciton generation rates in the EMLs of exciplex-forming co-host- and single host-based OLEDs at 4 V. (b) Drift-diffusion simulation results of the exciton generation rates assuming different EML mobility ratios. The hole and electron mobilities of each mobility ratio were as follows: $\mu_{\text{hole}} = 2 \times 10^{-8} \text{ cm}^2 \text{ V}^{-1} \text{ s}^{-1}$ and $\mu_{\text{electron}} = 2 \times 10^{-8} \text{ cm}^2 \text{ V}^{-1} \text{ s}^{-1}$ ($\gamma_{\text{mobility}}=1$), $\mu_{\text{hole}} = 2 \times 10^{-7} \text{ cm}^2 \text{ V}^{-1} \text{ s}^{-1}$ and $\mu_{\text{electron}} = 2 \times 10^{-8} \text{ cm}^2 \text{ V}^{-1} \text{ s}^{-1}$ ($\gamma_{\text{mobility}}=10$), $\mu_{\text{hole}} = 2 \times 10^{-7} \text{ cm}^2 \text{ V}^{-1} \text{ s}^{-1}$ and $\mu_{\text{electron}} = 2 \times 10^{-9} \text{ cm}^2 \text{ V}^{-1} \text{ s}^{-1}$ ($\gamma_{\text{mobility}}=100$), and $\mu_{\text{hole}} = 5 \times 10^{-7} \text{ cm}^2 \text{ V}^{-1} \text{ s}^{-1}$ and $\mu_{\text{electron}} = 5 \times 10^{-10} \text{ cm}^2 \text{ V}^{-1} \text{ s}^{-1}$ ($\gamma_{\text{mobility}}=1,000$).

Although the difference in EQE roll-off between the two devices was small, the corresponding difference in device lifetime was large because the quenching-induced degradation occurred continuously during operation. The correlation between the exciton generation rate distribution and the mobility balance was investigated by assuming different mobility ratios of 1, 10, 100, and 1,000 in the case when hole mobility was greater than electron mobility (Figure 3.4(b)). As the mobility ratio increased from 1 to 1,000, the distribution of the exciton generation rate moved toward the ETL side. Notably, when the mobility ratio exceeded 100, the exciton generation rate did not entirely cover the EML.

3.6 Conclusion

Enhancement of OLED device lifetime is governed by the internal accumulation of polarons. The capacitance–voltage characteristics of an exciplex-forming co-host-based OLED (device 1) and a single host-based OLED (device 2) were simulated and analyzed using drift-diffusion numerical modeling. The results showed that the difference in capacitance–voltage behaviors originated from a mobility difference between electrons and holes in the EMLs. The well-balanced mobilities of device 1 ($\gamma_{mobility} = 1.1$) resulted in a symmetric distribution of electrons and holes in the EML, which led to a broad recombination zone. However, a much greater hole mobility than electron mobility in the EML of device 2 ($\gamma_{mobility} = 1,136.4$) resulted in electron

accumulation at the interface between the EML and ETL because of retardation of electron transport toward EML. Therefore, the weighted recombination zone and high electron density in the EML accelerated exciton-exciton and exciton-polaron interactions and thereby reduced the operational stability of the OLED. Although the constituting materials were the same, the device lifetime of the exciplex-forming co-host-based OLED (device 1) was double that of the single host-based OLED (device 2), with no loss of efficiency. This result emphasizes the importance of considering mobility balance for realizing stable OLEDs. Many approaches have been reported to improve mobility balance in the EML, including the use of mixed-hosts, bipolar hosts, and different charge transport types of hosts and dopants. However, quantitative analysis of the mobility balance in hosts gives a better understanding of the correlation between the material systems and device performance. Finally, this physical insight provides an understanding of charge behavior in the devices that is essential to unraveling degradation mechanisms to enhance operational stability of OLEDs.

Chapter 4. Charge Transport Layers Manage Mobility and Carrier Density Balance in Light-emitting Layers Influencing the Operational Stability of Organic Light-emitting Diodes

4.1 Introduction

Organic light emitting diodes (OLEDs) have occupied a central position in practical applications, as a result of research and development by both academic research groups and industry. However, efforts to enhance the operational lifetimes of OLEDs continue to meet with significant challenges, owing to the complex mechanisms that underlie the associated degradation phenomena.^[24–26,104,125–127] It has been reported that organic materials gradually degrade to radical species through bond dissociation of molecules during operation.^[102,128–131] Several studies have shed light on the fundamental factors governing bond dissociation, and have proposed methods for managing these factors through the development of new materials and device structures.^[29,104,112,132–139] Organic materials in OLEDs are subject to polaronic and excitonic states resulting from charge injections from electrodes and recombination processes. Previous studies have indicated experimentally that the probability of bond dissociation is significantly increased not only by the instability inherent to polaronic and excitonic states, but also by the interaction between these two states.^{[30,105,106,140–}

^{142]} Various approaches, such as the use of graded doping concentrations,^[104] insertion of exciton-quenching material,^[111,112] and the use of co-doping sacrificial dopants,^[132] co-hosts^[33,138] or n-type hosts^[133] have been adopted with the aim of reducing exciton-polaron interaction and thereby attaining an improved lifetime. Notably, most approaches have focused on the light-emitting layer, despite the evident importance of the charge transport layer. Although some studies have examined the electrochemical stability of the charge transport layer, the requirements of the charge transport layer for operational stability have not yet been fully established.^[128,143,144]

In the present study, the effects of the hole transport layer (HTL) on device lifetime were investigated using impedance spectroscopy (IS). The static and dynamic behaviors of polarons in two different OLEDs, where device structure differed only in terms of the HTLs, demonstrated that HTLs serve to control the distribution of polaron density and the charge transport path in the light emitting layer (EML). Without altering the EML structure, hole mobility in the EML can be adjusted to achieve balanced electron and hole mobilities, by tuning the frontier orbital energies of HTL materials. Additionally, the hole density of the EML is balanced with the electron density according to charge accumulation at the HTL interface. This emphasizes the extent to which the electronic structure of the charge transport layers significantly affects operational stability via the mobility and carrier balance of the EML. This work indicates that comprehensive electrical analysis using single carrier devices and OLEDs can contribute significantly to the establishment of a design framework

for charge transport layers, where the goal is to improve device lifetime.

4.2 Experimental methods

The materials and device structures referred to in this paper are detailed in Figure 4.1. Organic materials, including N,N'-diphenyl-N,N'-bis-[4-(phenyl-m-tolyl-amino)-phenyl]-biphenyl-4,4'-diamine (DNTPD; Nichem, Taiwan), 9,9',9''-triphenyl-9H,9'H,9''H-3,3':6',3''-tercarbazole (TrisPCz; Nichem), 3,3-Di(9H-carbazol-9-yl)biphenyl (mCBP; Nichem), (4s,6s)-2,4,5,6-tetra(9H-carbazol-9-yl) isophthalonitrile (4CzIPN; Daejoo Electronic Materials, Korea), 3',3''',3''''-(1,3,5-triazine-2,4,6-triyl)tris([1,10-biphenyl]-3-carbonitrile) (CN-T2T; Lumtec, Taiwan), 9,10-bis(3-(pyridin-3-yl)phenyl) anthracene (DPyPA; Daejoo Electronic Materials), and 8,8'-spirobi[indolo[3,2,1-de]acridine] (H2; EM Index, Korea), were used as received without undergoing further purification.^[28,113,114,145] Pre-patterned 70 nm-thick indium tin oxide (ITO) glass was cleaned using deionized water, acetone, and isopropyl alcohol in sequence, and was subsequently used as the substrate. Organic layers were vacuum-deposited under a base pressure of $< 5 \times 10^{-8}$ Torr, following UV-ozone treatment of the substrate. The deposition rates of the organic layers were in the range of 0.5–1 Å/s. Following deposition, the samples were encapsulated with moisture getter in a glovebox.

The current density-voltage-luminance (J-V-L) and external quantum efficiencies were measured using a spectrometer (Photo Research PR650) and

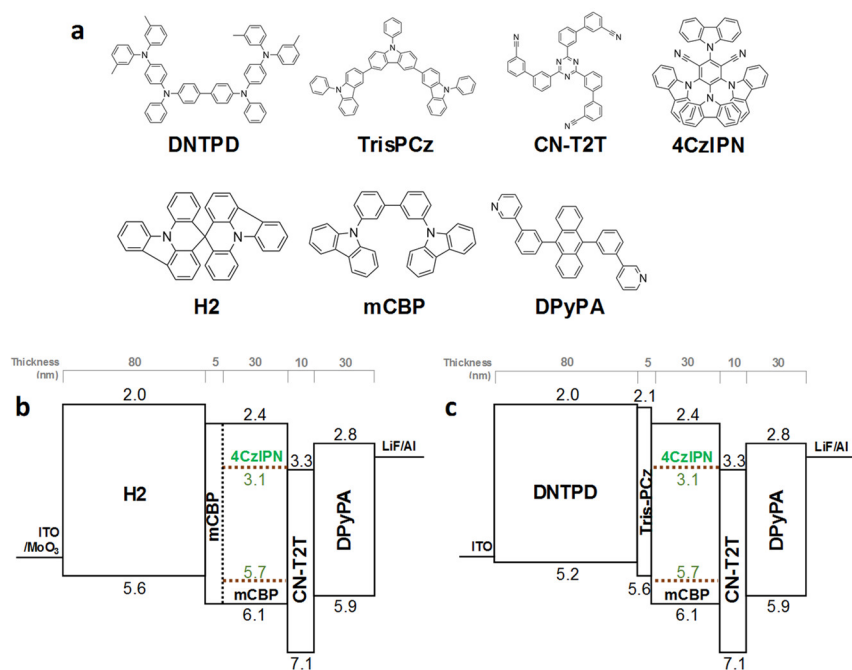


Figure 4.1 (a) Molecular structures of the materials used in organic light emitting diodes (OLEDs). (b; c) Structures of devices 1 and 2 showing the frontier orbital energy levels and thicknesses of the organic materials. (4s,6s)-2,4,5,6-tetra(9H-carbazol-9-yl) isophthalonitrile (4CzIPN)-doped 3,3-Di(9H-carbazol-9-yl)biphenyl (mCBP), 3',3''',3''''-(1,3,5-triazine-2,4,6-triyl)tris([1,10-biphenyl]-3-carbonitrile) (CN-T2T), and 9,10-bis(3-(pyridin-3-yl)phenyl) anthracene (DPyPA) are used as light emitting layer (EML), triplet/polaron blocking layer, and electron transporting layer.

a source meter (Keithley 2400). OLED lifetime was measured using the Polaronix M6000T lifetime measurement system. The current density of single carrier devices was measured by a source meter (Keithley 237) in dark conditions. Impedance analysis was performed with a Solartron Analytical moduLab XM. The amplitude of AC voltage was 100 mV, with the capacitance derived from Z' and Z'' , on the assumption that an organic semiconductor layer is electrically equivalent to a parallel RC circuit.

4.3 Device structure and performance of OLEDs

Two devices with different HTLs were fabricated to investigate the effects exerted on device lifetime by hole accumulation at the interface, and with different hole injection paths to an EML. The injection to the host molecules was followed by the trapping of dopant molecules, or direct injection of dopant into the EML. H2 and mCBP were used in device 1 as hole transporting materials (Figure 4.1b), while DNTPD and TrisPCz were used in device 2 (Figure 4.1c). The molecular structures of these materials are based on triphenylamine and carbazole moieties, which are electrochemically stable when in cation state. Highest occupied molecular orbital (HOMO) levels of the HTLs were -5.2 eV, -5.6 eV, -5.6 eV, and -6.1 eV for DNTPD, TrisPCz, H2, and mCBP, respectively. The other layers, including the EML [4CzIPN doped mCBP (15:85 in wt%)], the hole and triplet blocking layer (CN-T2T), and the electron transporting layer (ETL, DPyPA), were the same in both devices. A

green thermally activated delayed fluorescent material, 4CzIPN, was used as the emitting dopant. The alignment of the energy levels in the devices indicated that hole injection to the host material in the EML (mCBP) was expected in device 1. In contrast, direct hole injection to the dopant molecules was expected in device 2, especially when the doping concentration was high. The layers in close proximity to the EML were selected due to having higher triplet energies than those of the emitting dopant, to prevent the loss of excitons originating from the diffusion of triplet exciton in the EML into the adjacent layers.

The J-V-L, external quantum efficiency and power efficiency, and operational lifetime at an initial luminance of 1,000 cd/m² are illustrated in Figure 4.2, and the device performances are summarized in Table 4.1. The current density of device 1 was higher than that of device 2 after turn-on. The driving voltage of device 1 was also higher than that of device 2. For example, the driving voltage of device 1 at a luminance of 1,000 cd/m² was 4.0 V, lower than the 4.7 V recorded for device 2. Maximum EQEs and power efficiencies of the devices were 16.4 % and 61.6 lm/W for device 1, and 14.7 % and 36.5 lm/W for device 2. The EQE roll-off characteristics of each device also differed significantly. Device 1 exhibited a continuous decrease of EQE from 16.4 % as the current density was increased. However, the EQE of device 2 increased from 8.2 % at 1.2×10^{-2} mA/cm² to 14.7 % at 1.2 mA/cm², while decreasing at higher current densities. This increase in EQE is attributed to the increase in the charge balance factor, since photo luminescence quantum yield (PLQY), dipole orientation, and out-coupling efficiency all remained constant independent of the current

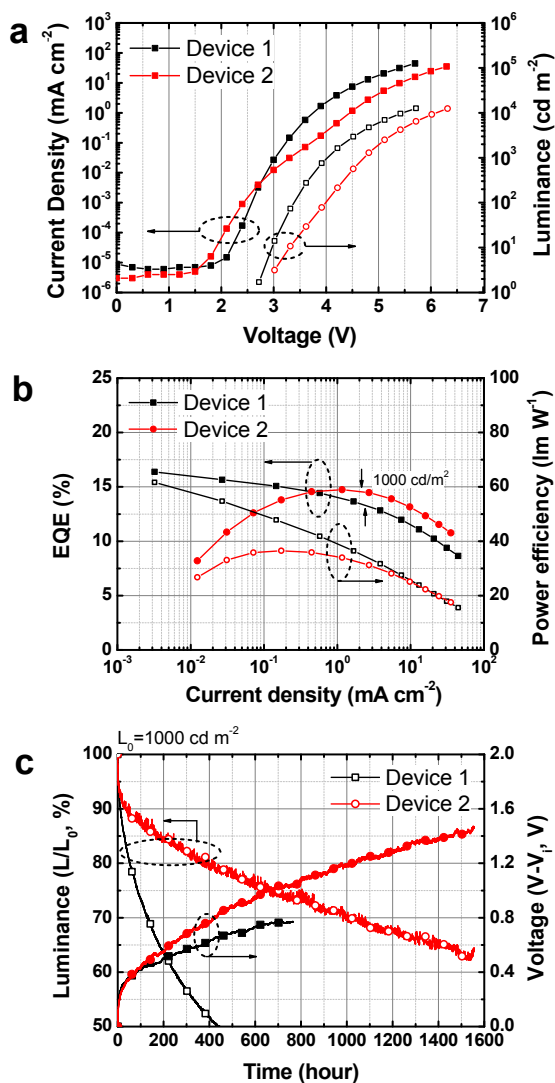


Figure 4.2 (a) Current-density-voltage-luminance, (b) external quantum efficiency-power efficiency-luminance, and (c) luminance-voltage changes over the duration of the operation (L-V-t) of OLEDs. L-V-t is measured under the constant current condition at an initial luminance of $1,000 \text{ cd/m}^2$. The driving voltages at $1,000 \text{ cd/m}^2$ are 4.0 V for device 1 and 4.7 V for device 2.

	EQE (%)		Current efficiency (cd/A)		Power efficiency (lm/W)		Turn-on Voltage (V)	LT80 (hour)
	Max	1000 cd/m ²	Max	1000 cd/m ²	Max	1000 cd/m ²		
Device 1	16.4	13.7	53.0	45.2	61.6	36.4	2.7	52
Device 2	14.7	14.5	48.6	47.7	36.5	31.2	3.0	357

Table 4.1 Performances and lifetimes of devices 1 and 2.

density. The higher power efficiency of device 1 in comparison to that of device 2 is attributed to the lower driving voltage of the former device at the same current density. Given these device characteristics, the efficiencies of device 1 are almost equivalent to those of device 2 at 1,000 cd/m² (~2 mA/cm²). However, the operational lifetime of device 2 at the initial luminance of 1,000 cd/m² was around seven times that of device 1, as illustrated in Figure 4.2c. Device 1 had an LT80 of 52 hours while that of device was 357 hours, where LT80 is defined as the timespan over which the luminance of the device decreases to 80 % of its initial value.

4.4 Charge transport in single carrier devices

Toward a fuller understanding of the reasons behind the significant difference in lifetime between the two devices, the hole and electron transports in the devices were analyzed by IS using single carrier devices. The field-dependent hole mobilities of the HTLs of H2, mCBP, DNTPD and TrisPCz were measured using the corresponding hole-only-devices (HODs) of ITO/HTLs/Al, where the HTLs are MoO₃ (1 nm)/H2 (100 nm), MoO₃ (1 nm)/H2 (10 nm)/mCBP (100 nm), DNTPD (100 nm), and DNTPD (10 nm)/TrisPCz (100 nm). The thin MoO₃ (1 nm), MoO₃ (1 nm)/H2 (10 nm) or DNTPD (10 nm) layers in the devices were used to form an Ohmic contact for hole injection to the HTLs. Additionally, charge transport in the EML was analyzed using the following half-devices:

Hole-only half-device (HOHD) 1;

ITO/MoO₃ (1 nm)/H2 (10 nm)/mCBP (5 nm)/EML (100 nm)/DNTPD (30 nm)/Al

HOHD 2;

ITO/DNTPD (10 nm)/TrisPCz (5 nm)/EML (100 nm)/DNTPD (30 nm)/Al

Electron-only half-device (EOHD);

ITO/DPyPA (30 nm)/EML (100 nm)/CN-T2T (5 nm)/DPyPA (10 nm)/LiF (1 nm)/Al.

The thin DNTPD layer was inserted between the EML and the Al electrode in the HOHDs to block the electron injection from the Al electrode. Similarly, the thin DPyPA layer was inserted between the ITO and EML layers of the EOHD to block the hole injection from the ITO.

The extraction of field-dependent mobilities may be achieved with the application of two different IS methods: negative differential susceptance ($-AB-f$) or an imaginary Z ($Z''-f$) spectrum.^[34,35,37,39,122,146–153] A $Z''-f$ method was selected for this study, as this method is not dependent on the extent of the dispersive charge transport in organic semiconductors.^[37] Figures 4.3a and b illustrate the $Z''-f$ spectra of the HOHDs. (The $Z''-f$ spectra of the HODs and the EOHD are illustrated in the supporting information.) The peak frequency, or the characteristic frequency in the spectrum of HOHD 1, shifted from 150 kHz at 6.0 V to 480 kHz at 7.0 V. In contrast, the peak frequency of HOHD 2 was very low and also shifted from 14 Hz at 7 V to 84 Hz at 8 V. The shift in the peak frequency following the application of DC voltage is attributed to the

field-dependent mobility of organic semiconductors, where the peak frequency is related to the mobility by the following equation:^[34–36,154,155]

$$f_{\max} = \kappa \tau_{tr}^{-1} \quad (4.1)$$

$$\mu = \frac{d^2}{\tau_{tr} V} \quad (4.2)$$

f_{\max} , κ , τ_{tr} , μ , d , and V are the peak frequency, numerical coefficient, average transit time, charge carrier mobility, thickness of the active layer, and DC voltage, respectively. The coefficient κ is used as 0.44, which was determined from analytic simulation assuming the space charge-limited current and moderate dispersion of hopping transport.^[37] The mobilities determined from the characteristic frequencies of the Z'' - f spectra are illustrated in Figure 4.3c. The hole mobilities of the HTLs used in the OLEDs are significantly different, and the values are in the order DNTPD > H2 > mCBP > TrisPCz. It is interesting to note that the effective hole mobilities obtained from HOHD 1 and 2 vary, considering that only the HTLs differed, while the EML thickness was 100 nm in both. The effective hole mobility of HOHD 1 is $6.1 \times 10^{-5} \text{ cm}^2 \text{ V}^{-1} \text{ s}^{-1}$ at the electric field of 0.7 MV/cm, which is four orders of magnitude greater than that of HOHD 2 ($1.8 \times 10^{-9} \text{ cm}^2 \text{ V}^{-1} \text{ s}^{-1}$) at the same electric field. Considering the much higher mobilities and the thinness of the HOHD's HTLs, the mobility differences

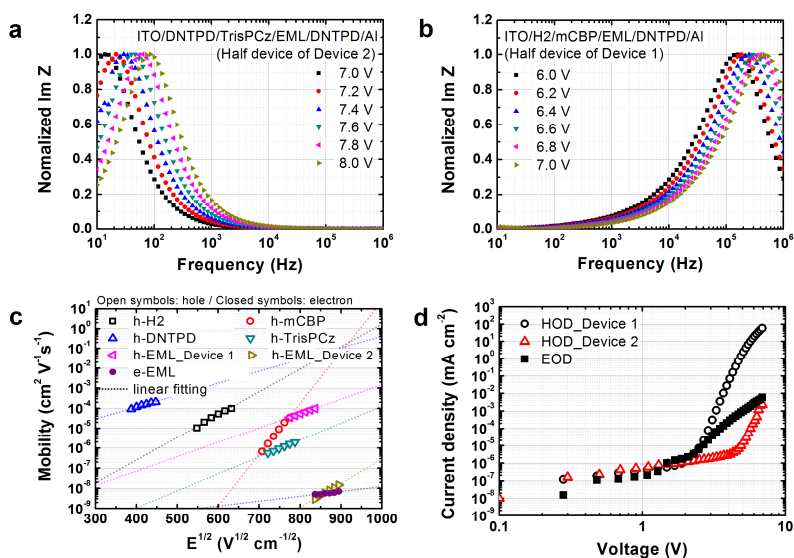


Figure 4.3 DC voltage-dependent imaginary Z-frequency spectrums of hole-only half-devices of (a) device 1 and (b) device 2. The transit time of the charge carrier in the charge-only device is determined from the peak frequency of Z'' -f spectrums. (c) Field-dependent electron and hole mobilities of hole transporting layers (HTLs) and EMLs. Regarding EML hole mobility, although 100 nm of the EML layer is the same in devices 1 and 2, mobility varies when the HTLs are changed. The dotted lines indicate linear fitting results. (d) Current density-voltage characteristics of charge-only devices consisting of the EML.

between the devices can be attributed to the differences in hole mobilities in the EML. This result clearly demonstrates that the charge transport in the EML is highly dependent on the HTLs; more specifically, it depends on the energy level alignment between the charge transporting layer and the host and dopant energy levels in the EML. In device 1, the holes in the EML are expected to transport mCBP and 4CzIPN through HOMO simultaneously, since the adjacent hole-transporting layer is intrinsic mCBP layer. However, holes in the EML of device 2 mainly transported 4CzIPN through HOMO via long-range hopping, because the energetic barrier between TrisPCz and mCBP is 0.5 eV. The detrapping of holes from 4CzIPN to mCBP is difficult, owing to the large trap depth of 0.45 eV. Meanwhile, the electrons in the EML exhibit low mobility of $3.2 \times 10^{-9} \text{ cm}^2 \text{ V}^{-1} \text{ s}^{-1}$ at the electric field of 0.7 MV/cm. This low electron mobility in the EML is caused by the charge transport of 4CzIPN molecules by hopping through the lowest unoccupied molecular orbital (LUMO) level. It is noteworthy that the electron and hole mobilities in the EML of device 2 are almost the same, indicating that electrons and holes share the same transport path. The mobility ratios, defined as the ratio of hole mobility to electron mobility, are 1.9×10^4 for device 1 and 1.7 for device 2. It has been reported that the degree of charge balance can be enhanced through the adoption of bipolar host or co-host (i.e., the use of both p- and n-type hosts) structures.^[33,156,157] These findings also imply that the mobility in the EML can be managed by inducing the charge to transport through the frontier orbitals of the host or dopant molecules without alteration of the EML materials.

J-V characteristics of the single carrier devices comprising the EML are compared in Figure 4.3d. The current density of device 1's HOHD is shown to significantly increase at a voltage of 2.5 V, and reaches 6.0×10^1 mA/cm² at 7.0 V. The HOHD of device 2 exhibits a current density in the order of 10^{-6} mA/cm² up to 5.0 V, and increases up to 3.0×10^{-3} mA/cm² at 7.0 V. In the case of the EOHD, the current density increases from 7.2×10^{-6} mA/cm² at 2.5 V to 7.5×10^{-3} mA/cm² at 7V. At 7–8 V, the current density levels in the EOHD and HOHD of device 2 are within the same range. Since the current density is proportional to the mobility and carrier density of the device, these findings indicate that the carrier balance, in terms of both the mobility and the carrier density, is well-adjusted in device 2.

4.5 Impedance analysis of the OLEDs

The impedance response of the OLEDs was analyzed from the perspective of their capacitance-voltage (*C-V*) and capacitance-frequency (*C-f*) characteristics. Several factors cause increases or decreases in the capacitances of the OLEDs. First, charge accumulation between layers increases the capacitance, as space charges transporting in the organic layer can accumulate due to the energetic barrier between layers or abrupt retardation of the mobility.^[42,40,41] Second, the trapping/detrapping responses of a charge also triggers an increase in the capacitance.^[43–46] In the EML adopting host-dopant structure, the dopants may be considered, from an energetic perspective, to function as an electrical trap,

since one of the frontier orbital levels of the dopants is usually located in the host's bandgap. In the case of a 4CzIPN-doped mCBP host, the 4CzIPN molecules function simultaneously as electron and hole traps. Third, a charge recombination of electrons and holes contributes to a reduction in capacitance. This is understood as extinction of the charges via exciton formation and the decay to ground state. In light of this, the minimum capacitance value can theoretically be expected to be zero, if the remaining charge density equals zero. However, several instances wherein OLEDs have exhibited negative capacitance with increasing luminance have been reported.^[42,40,47-50] Although negative capacitance of OLED has been the focus of a number of studies, a full understanding of the phenomenon remains elusive.^[47-50] The capacitance is the result of simultaneous contributions from these mechanisms.

The C-V characteristics of the OLEDs are illustrated along with J-V-L in Figure 4.4a. The frequency of the AC voltage is constant at 50 Hz. At 0 V, the initial capacitances of the OLEDs are affected by diffusion charge only, in the absence of the injection of a drift charge from the electrodes. The initial capacitances of both devices are 0.93 nF and 0.96 nF and are close to the calculated geometrical capacitance of 0.91 nF, assuming a total thickness of 150 nm and a dielectric constant of 3.85. In both devices, therefore, the effect of a diffusion charge on the initial capacitance can be ruled out. As the voltage increases, the capacitance of device 1 gradually increases from the geometrical capacitance to reach the peak capacitance of 6.4 nF at 4.1 V, and the capacitance decreases steadily as voltage is increased. The capacitance of device 2 increases to 4.6 nF at 3.5 V

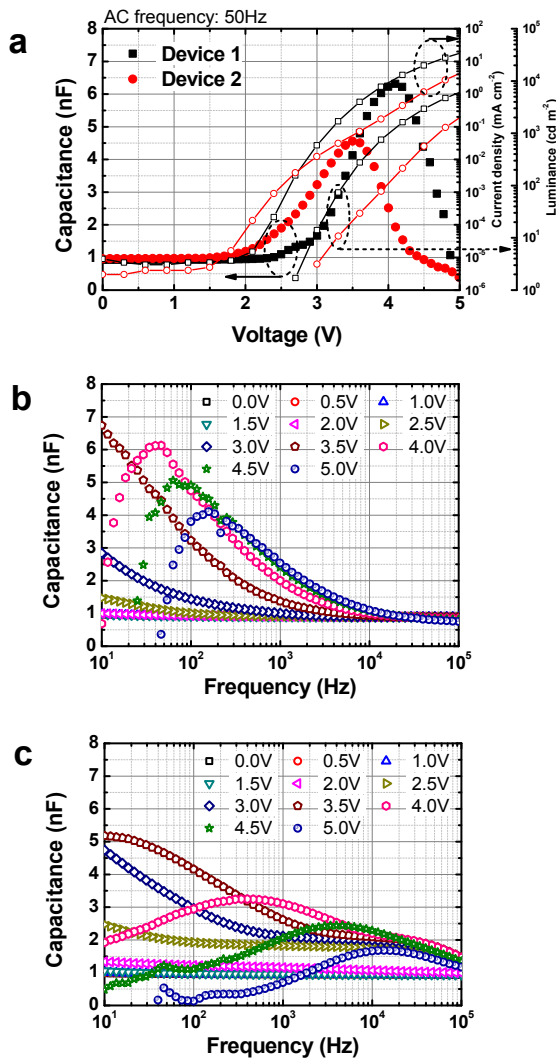


Figure 4.4 (a) Parallel capacitance-voltage at an AC frequency of 50 Hz with current density-voltage-luminance (J-V-L) and (b; c) capacitance-frequencies for various DC voltages of devices 1 and 2. The amplitude of AC voltage is 100 mV. Regarding charge transport in the OLEDs, the capacitance is a result of the total contribution of charge accumulation at the interface, trapping/detrapping responses due to the dopant in the EML, and recombination.

and then also decreases as the voltage increases.

To clarify the origins of the C - V characteristics, the C - f characteristics at different DC voltages were measured. These are depicted in Figure 4.4b and c for devices 1 and 2, respectively. The capacitance in device 1 is seen to increase steadily as the frequency decreases. The continuous elevation in capacitance is due to the contribution made by the trapping/detrapping response of the charges.^[44–46] It can be observed that the capacitance continuously increases beyond even the turn-on voltages, for example, at 3.0 and 3.5 V. This indicates that, although some of the trapped holes of 4CzIPN recombine with electrons, the remaining holes de-trap from dopant to host, thereby contributing to the capacitance. At higher voltages than 3.5 V, the capacitance decreases as frequency decreases below certain critical frequencies, depending on the applied voltage. The C - f characteristics of device 2 differ significantly to those of device 1. At 2.5 V, the C - f spectrum exhibits a plateau region in the frequency range of 10^2 – 10^4 Hz with a capacitance increase in the range of 10^1 – 10^2 Hz. The plateau region may be attributed to the charge accumulation at the interface between DNTPD and TrisPCz, owing to mobility retardation and the energetic barrier. The capacitance will exhibit a plateau in low frequency regions with transition frequency, as the majority of accumulated charges react with oscillating voltages lower than a specific frequency corresponding to transit time. A plateau caused by charge accumulation may be considered a double parallel RC circuit where there is significant difference between R1 and R2.^[42] The analysis is also supported by the capacitance value of 1.8 nF in the plateau

region, and its proximity to the calculated value of 1.8 nF, assuming a thickness of 75 nm. At voltages exceeding 2.5 V, the frequencies that begin to increase the capacitance are elevated, owing to the increasing mobility of the holes. The contribution of the recombination process gradually increases with increasing voltage, reducing the capacitance if the voltage exceeds 3.5 V.

4.6 Correlation between the charge transport and operational stability of the OLEDs

Following comprehensive electrical analysis of OLEDs and single carrier devices, electrical characteristics such as charge accumulation, transport and recombination across both devices can be discussed and correlated with the operational stability of the devices. Toward a fuller understanding, the capacitance-luminance ($C-L$) at a frequency of 50 Hz, and $C-f$ at a luminance of 1,000 cd/m^2 are compared in Figure 4.5a and b. The increase in capacitance of device 1 in $C-L$ and $C-f$ (Figure 4.5a) originates from the trapping/detrapping responses of holes in the EML; this is verified by the increasing capacitance relative to decreasing frequency above the turn-on voltage (Figure 4.4b). The fact that hole mobility exceeded electron mobility (Figure 4.3c), and that the hole current was greater than the electron current (Figure 4.3d), both corroborate the observation that holes transport through host molecules, and that hole trapping in the EML makes a major contribution to capacitance. At luminance in excess of 1,000 cd/m^2 , increasing numbers of electrons are

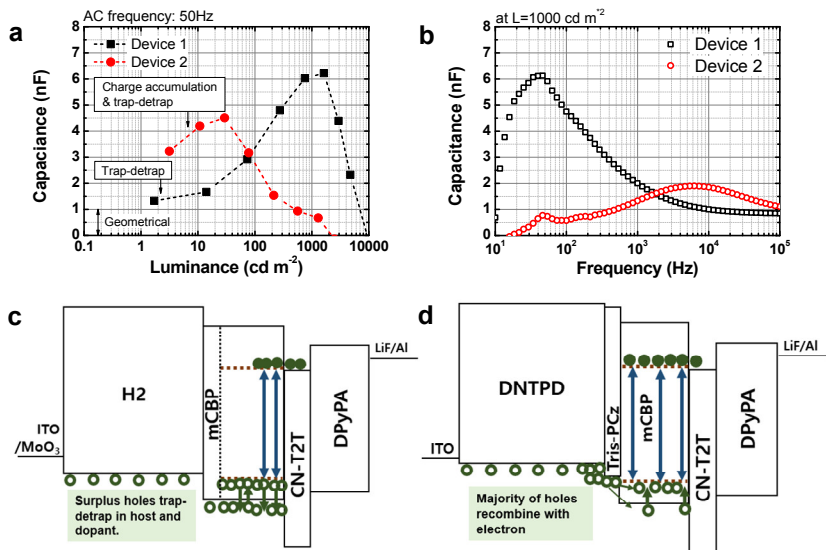


Figure 4.5 (a) Capacitance of devices 1 and 2 depending on luminance. (b) Capacitance-frequency of devices 1 and 2 at a luminance of 1,000 cd/m^2 . The driving voltage at 1,000 cd/m^2 is 4.0 V and 4.7 V for devices 1 and 2, respectively. (c; d) Schematic illustration showing the transport of electrons and holes in devices 1 and 2 at 1,000 cd/m^2 based on impedance analysis.

injected and these recombine with the trapped holes (reduction of capacitance at low frequency is illustrated in Figure 4.4b). In contrast to device 1, both the charge accumulation at the DNTPD/TrisPCz interfaces (the plateau region illustrated in Figure 4.4c), and the trapping/detrapping responses (i.e., the increase of capacitance at low frequency following turn-on) occur to produce high capacitance at low luminance in device 2 (Figure 4.5a). Very low mobilities of electrons and holes in the EML reveal that both electrons and holes transport between dopant molecules. At luminance in excess of 30 cd/m^2 , electron and hole injection to the dopant molecules increases significantly to reduce accumulation at the interfaces (reduction of capacitance is illustrated in Figure 4.5a, and reduction of capacitance in the low frequency region at high voltages is shown in Figure 4.4c). The balanced electron and hole mobilities in the EML of device 2 (Figure 4.3c) indicate good charge balance in the EML, which contributes to the reduction of capacitance below the geometrical capacitance. (Figure 4.5b). Figure 4.5c and d present schematic diagrams illustrating the charge dynamics at $1,000 \text{ cd/m}^2$ in the OLEDs. In device 1, holes in the EML recombine with electrons, but there are surplus holes in the mCBP and 4CzIPN molecules. From 10^4 times higher hole mobility than electron mobility, it is expected that the recombination zone is located toward EML/ETL interface.^[33] Consequently, the positive polaronic states of mCBP and 4CzIPN are excited to high energy states by adjacent excited molecules, resulting in an increased probability of bond dissociation. In contrast, some of the injected holes of device 2 accumulate at the DNTPD/TrisPCz interface, with a small

number of holes simultaneously injected with 4CzIPN and mCBP. The majority of the injected holes of the EML recombine with electrons. Balanced electron and hole mobilities lead to broad recombination zone. Therefore, the quantity of polarons present in mCBP and 4CzIPN during the operation of device 2 is relatively low in comparison with device 1.

This observation points the way toward the development of a new method for prolonging the lifetimes of OLEDs, simply by tuning the energy levels and mobilities of the HTL and ETL without altering the emitting layers. Accordingly, the polaron transport is managed, facilitating tuning of the polaron densities and transporting paths, and of the recombination processes in the EML, thereby increasing device lifetime.

4.7 Conclusion

We have demonstrated that charge transport layers fulfil important roles in managing and controlling carrier density and tuning the transport path to the EML. By simply modifying the HTLs in device structures, device lifetime is increased sevenfold at an initial luminance of 1,000 cd/m². Factors contributing to this improvement were identified as a variety of electrical characterizations of single carrier devices and OLEDs. The results strongly indicate that frontier orbital energy level alignment should be considered for all organic layers, with adjustment of the mobility and carrier density of the EML. Additionally, the impedance analysis carried out in this study contributes to our understanding of

the mechanisms underlying in-operation charge transport, such as charge accumulation, charge trapping, and recombination. Longer-lived OLEDs may be achieved through balancing mobility and carrier density in the EML, which is facilitated by combining the emitting layer and charge transport layers.

Chapter 5. Summary and Conclusion

In this dissertation, charge generation process of electrically doped organic semiconductors and polaron behavior of OLEDs for operational stability is explored. In **chapter 2**, charge generation process of Rb_2CO_3 -doped TPBi is investigated. Charge generation process is divided into the charge transfer complex (CTC) formation and dissociation to free charge carrier. Based on the understanding, quantitative analysis of CTC formation efficiency and dissociation efficiency is performed. From UV-Vis-NIR spectroscopy and Mott-Schottky analysis, the number of charge transfer complexes and free charge carriers in doped organic semiconductors is characterized. Interestingly, the CTC formation efficiency is in the range of 47.0~82.8% in the doping concentration we investigated. The dissociation efficiency is in the range of 1~4%. This result indicates that formation of charge transfer complex is relatively efficient compared to dissociation into free charge carriers in organic semiconductors considering a few percents of charge generation efficiency.

In chapter 3 and 4, device stability of OLEDs is understood by an analysis of polaron behavior via various electrical characterizations and drift-diffusion numerical simulation. In **chapter 3**, by comparison of exciplex-forming co-host based OLED and single host-based OLED, it is demonstrated that mobility balance in the EML, which is a balance between electron and hole mobility, is a crucial factor in the stability of OLEDs. From drift-diffusion numerical modeling, mobility balance in the EML governs the distribution of exciton and

polaron density which is the main origin of material degradation. This analysis shows that quantitative characterization of charge carrier mobility in the EML is important to enhance device stability even though co-host or bipolar host is adopted. In **chapter 4**, the role of the charge transport layer in the operational stability of OLEDs is revealed. For the realization of long-lived OLEDs, the design of charge transport layers is a crucial point in addition to the light-emitting layer since polarons transport through charge transport layers. In the experiment, by changing the HTLs only in the device structure, device lifetime is seven-times enhanced. A variety of electrical characterization of single-carrier devices and OLEDs reveal that charge transport layer acts as a manager controlling charge density in the EML via energetic barrier and acts as a guide inducing charge transport path in the EML via energetics between HTL and EML. Consequently, it is demonstrated that the charge transport layer affects charge balance in term of mobility balance and carrier density balance.

In conclusion, electrical characterization of organic semiconductors and OLEDs is necessary to understand charge behavior and device stability. Elucidation of charge generation mechanism of doped organic semiconductors will lead to fine-tuned carrier density from the established theoretical model. Doping technology based on fundamental understanding will enable organic electronic devices to be efficient by controlling carrier density and the Fermi level.

From experiments and modeling, it is verified that understanding of polaron

behavior is important to find a way for a long lifetime of OLED in addition to the use of electrochemically stable materials. Since degradation of OLEDs is governed by complicated mechanisms concerning materials and device structures, comprehensive consideration of both the chemical durability of materials and polaron-exciton behavior should be performed to realize long-lived OLEDs.

Bibliography

- [1] X. Zhou, J. Blochwitz, M. Pfeiffer, A. Nollau, T. Fritz, K. Leo, *Adv. Funct. Mater.* **2001**, *11*, 310.
- [2] J. Huang, M. Pfeiffer, A. Werner, J. Blochwitz, K. Leo, S. Liu, *Appl. Phys. Lett.* **2002**, *80*, 139.
- [3] D.-S. Leem, H.-D. Park, J.-W. Kang, J.-H. Lee, J. W. Kim, J.-J. Kim, *Appl. Phys. Lett.* **2007**, *91*, 11113.
- [4] D.-S. Leem, S.-Y. Kim, J.-J. Kim, M.-H. Chen, C.-I. Wu, *Electrochem. Solid-State Lett.* **2009**, *12*, J8.
- [5] H.-S. Shim, S.-Y. Kim, J. Whan Kim, T.-M. Kim, C.-H. Lee, J.-J. Kim, *Appl. Phys. Lett.* **2013**, *102*, 203903.
- [6] D.-H. Kim, T.-M. Kim, W.-I. Jeong, J.-J. Kim, *Appl. Phys. Lett.* **2012**, *101*, 153303.
- [7] Y. Abe, T. Hasegawa, Y. Takahashi, T. Yamada, Y. Tokura, *Appl. Phys. Lett.* **2005**, *87*, 153506.
- [8] C. Liu, J. Jang, Y. Xu, H.-J. Kim, D. Khim, W.-T. Park, Y.-Y. Noh, J.-J. Kim, *Adv. Funct. Mater.* **2015**, *25*, 758.
- [9] J. H. Lee, J. J. Kim, *Phys. Status Solidi Appl. Mater. Sci.* **2012**, *209*, 1399.
- [10] S. J. Yoo, J. J. Kim, *Macromol. Rapid Commun.* **2015**, *36*, 984.
- [11] J. H. Lee, D. S. Leem, H. J. Kim, J. J. Kim, *Appl. Phys. Lett.* **2009**, *94*, 2009.

- [12] J. H. Lee, D. S. Leem, J. J. Kim, *Org. Electron. physics, Mater. Appl.* **2010**, *11*, 486.
- [13] J. H. Lee, H. M. Kim, K. B. Kim, R. Kabe, P. Anzenbacher, J. J. Kim, *Appl. Phys. Lett.* **2011**, *98*, 8.
- [14] J. H. Lee, H. M. Kim, K. B. Kim, J. J. Kim, *Org. Electron. physics, Mater. Appl.* **2011**, *12*, 950.
- [15] P. Pingel, D. Neher, *Phys. Rev. B - Condens. Matter Mater. Phys.* **2013**, *87*, 1.
- [16] I. Salzmann, G. Heimel, S. Duhm, M. Oehzelt, P. Pingel, B. M. George, A. Schnegg, K. Lips, R. P. Blum, A. Vollmer, N. Koch, *Phys. Rev. Lett.* **2012**, *108*, 1.
- [17] S. J. Yoo, J. H. Lee, J. H. Lee, J. J. Kim, *Appl. Phys. Lett.* **2013**, *102*.
- [18] S.-J. Yoo, J.-H. Lee, J.-M. Kim, J.-J. Kim, *Appl. Phys. Lett.* **2017**, *110*, 53303.
- [19] C. W. Tang, S. A. VanSlyke, *Appl. Phys. Lett.* **1987**, *51*, 913.
- [20] K. S. Yook, J. Y. Lee, *Adv. Mater.* **2012**, *24*, 3169.
- [21] D. Huang, C. Wang, Y. Zou, X. Shen, Y. Zang, H. Shen, X. Gao, Y. Yi, W. Xu, C. A. Di, D. Zhu, *Angew. Chemie - Int. Ed.* **2016**, *55*, 10672.
- [22] H. Sasabe, J. Kido, *J. Mater. Chem. C* **2013**, *1*, 1699.
- [23] K.-H. Kim, J.-J. Kim, *Adv. Mater.* **2018**, 1705600.
- [24] H. Aziz, Z. D. Popovic, *Chem. Mater.* **2004**, *16*, 4522.
- [25] A. Turak, *RSC Adv.* **2013**, *3*, 6188.

- [26] S. Scholz, D. Kondakov, B. Lüsse, K. Leo, *Chem. Rev.* **2015**, *115*, 8449.
- [27] W. Song, J. Y. Lee, *Adv. Opt. Mater.* **2017**, *5*, 1600901.
- [28] H. Uoyama, K. Goushi, K. Shizu, H. Nomura, C. Adachi, *Nature* **2012**, *492*, 234.
- [29] H. Nakanotani, K. Masui, J. Nishide, T. Shibata, C. Adachi, *Sci. Rep.* **2013**, *3*, 2127.
- [30] A. S. D. Sandanayaka, T. Matsushima, C. Adachi, *J. Phys. Chem. C* **2015**, *119*, 23845.
- [31] M. Kim, S. K. Jeon, S. H. Hwang, J. Y. Lee, *Adv. Mater.* **2015**, *27*, 2515.
- [32] D. Zhang, M. Cai, Y. Zhang, D. Zhang, L. Duan, *Mater. Horiz.* **2016**, *3*, 145.
- [33] J.-M. Kim, C.-H. Lee, J.-J. Kim, *Appl. Phys. Lett.* **2017**, *111*, 203301.
- [34] S. W. Tsang, S. K. So, J. B. Xu, *J. Appl. Phys.* **2006**, *99*, 13706.
- [35] T. Okachi, T. Nagase, T. Kobayashi, H. Naito, *Jpn. J. Appl. Phys.* **2008**, *47*, 8965.
- [36] N. D. Nguyen, M. Schmeits, H. P. Loebel, *Phys. Rev. B* **2007**, *75*, 75307.
- [37] D. C. Tripathi, A. K. Tripathi, Y. N. Mohapatra, *Appl. Phys. Lett.* **2011**, *98*, 33304.
- [38] J. H. Lee, J. Lee, Y. H. Kim, C. Yun, B. Lüsse, K. Leo, *Org. Electron. physics, Mater. Appl.* **2014**, *15*, 16.

- [39] K. Takagi, S. Abe, T. Nagase, T. Kobayashi, H. Naito, *J. Mater. Sci. Mater. Electron.* **2015**, *26*, 4463.
- [40] C. Weichsel, L. Burtone, S. Reineke, S. I. Hintschich, M. C. Gather, K. Leo, B. Lüssem, *Phys. Rev. B* **2012**, *86*, 75204.
- [41] Y. H. Deng, Y. Q. Li, Q. D. Ou, Q. K. Wang, F. Z. Sun, X. Y. Chen, J. X. Tang, *Org. Electron.* **2014**, *15*, 1215.
- [42] S. Nowy, W. Ren, A. Elschner, W. Lövenich, W. Brütting, *J. Appl. Phys.* **2010**, *107*, 54501.
- [43] J. Bisquert, *Phys. Rev. B* **2008**, *77*, 235203.
- [44] L. Burtone, D. Ray, K. Leo, M. Riede, *J. Appl. Phys.* **2012**, *111*, 64503.
- [45] L. Burtone, J. Fischer, K. Leo, M. Riede, *Phys. Rev. B* **2013**, *87*, 45432.
- [46] P. Pahner, H. Kleemann, L. Burtone, M. L. Tietze, J. Fischer, K. Leo, B. Lüssem, *Phys. Rev. B* **2013**, *88*, 195205.
- [47] E. Ehrenfreund, C. Lungenschmied, G. Dennler, H. Neugebauer, N. S. Sariciftci, *Appl. Phys. Lett.* **2007**, *91*, 12112.
- [48] L. Zhang, H. Nakanotani, C. Adachi, *Appl. Phys. Lett.* **2013**, *103*, 93301.
- [49] M. Takata, K. Takagi, T. Nagase, T. Kobayashi, H. Naito, *J. Nanosci. Nanotechnol.* **2016**, *16*, 3322.
- [50] M. Guan, L. Niu, Y. Zhang, X. Liu, Y. Li, Y. Zeng, *RSC Adv.* **2017**, *7*, 50598.

- [51] B. Lussem, M. Riede, K. Leo, *Doping of organic semiconductors*; 2013; Vol. 210.
- [52] H. Méndez, G. Heimel, A. Opitz, K. Sauer, P. Barkowski, M. Oehzelt, J. Soeda, T. Okamoto, J. Takeya, J. B. Arlin, J. Y. Balandier, Y. Geerts, N. Koch, I. Salzmann, *Angew. Chemie - Int. Ed.* **2013**, *52*, 7751.
- [53] I. Salzmann, G. Heimel, S. Duhm, M. Oehzelt, P. Pingel, B. M. George, A. Schnegg, K. Lips, R. P. Blum, A. Vollmer, N. Koch, *Phys. Rev. Lett.* **2012**, *108*, 1.
- [54] B. Bernardo, D. Cheyons, B. Verreet, R. D. Schaller, B. P. Rand, N. C. Giebink, *Nat. Commun.* **2014**, *5*, 1.
- [55] A. Mityashin, Y. Olivier, T. Van Regemorter, C. Rolin, S. Verlaak, N. G. Martinelli, D. Beljonne, J. Cornil, J. Genoe, P. Heremans, *Adv. Mater.* **2012**, *24*, 1535.
- [56] M. L. Tietze, P. Pahner, K. Schmidt, K. Leo, B. Lussem, *Adv. Funct. Mater.* **2015**, *25*, 2701.
- [57] M. L. Tietze, L. Burtone, M. Riede, B. Lussem, K. Leo, *Phys. Rev. B - Condens. Matter Mater. Phys.* **2012**, *86*, 1.
- [58] I. Salzmann, G. Heimel, M. Oehzelt, S. Winkler, N. Koch, *Acc. Chem. Res.* **2016**, *49*, 370.
- [59] C. K. Chan, E. G. Kim, J. L. Brédas, A. Kahn, *Adv. Funct. Mater.* **2006**, *16*, 831.
- [60] Y. Qi, T. Sajoto, S. Barlow, E. G. Kim, J. L. Brédas, S. R. Marder, A.

- Kahn, *J. Am. Chem. Soc.* **2009**, *131*, 12530.
- [61] S. Olthof, W. Tress, R. Meerheim, B. Lüsse, K. Leo, *J. Appl. Phys.* **2009**, *106*.
- [62] J. Meyer, S. Hamwi, S. Schmale, T. Winkler, H.-H. Johannes, T. Riedl, W. Kowalsky, *J. Mater. Chem.* **2009**, *19*, 702.
- [63] M. Kröger, S. Hamwi, J. Meyer, T. Riedl, W. Kowalsky, A. Kahn, *Org. Electron. physics, Mater. Appl.* **2009**, *10*, 932.
- [64] R. Meerheim, S. Olthof, M. Hermenau, S. Scholz, A. Petrich, N. Tessler, O. Solomeshch, B. Lüsse, M. Riede, K. Leo, *J. Appl. Phys.* **2011**, *109*.
- [65] S. Olthof, S. Mehraeen, S. K. Mohapatra, S. Barlow, V. Coropceanu, J. L. Brédas, S. R. Marder, A. Kahn, *Phys. Rev. Lett.* **2012**, *109*, 1.
- [66] T. Menke, D. Ray, H. Kleemann, M. P. Hein, K. Leo, M. Riede, *Org. Electron. physics, Mater. Appl.* **2014**, *15*, 365.
- [67] Y. H. Lou, M. F. Xu, L. Zhang, Z. K. Wang, S. Naka, H. Okada, L. S. Liao, *Org. Electron. physics, Mater. Appl.* **2013**, *14*, 2698.
- [68] A. Higgins, S. K. Mohapatra, S. Barlow, S. R. Marder, A. Kahn, *Appl. Phys. Lett.* **2015**, *106*, 1.
- [69] T. Glaser, S. Beck, B. Lunkenheimer, D. Donhauser, A. Köhn, M. Kröger, A. Pucci, *Org. Electron. physics, Mater. Appl.* **2013**, *14*, 575.
- [70] B. D. Naab, S. Zhang, K. Vandewal, A. Salleo, S. Barlow, S. R. Marder, Z. Bao, *Adv. Mater.* **2014**, *26*, 4268.
- [71] D. T. Duong, H. Phan, D. Hanifi, P. S. Jo, T. Q. Nguyen, A. Salleo,

- Adv. Mater.* **2014**, *26*, 6069.
- [72] J. Zhao, Y. Cai, J. P. Yang, H. X. Wei, Y. H. Deng, Y. Q. Li, S. T. Lee, J. X. Tang, *Appl. Phys. Lett.* **2012**, *101*.
- [73] K. R. Choudhury, J. H. Yoon, F. So, *Adv. Mater.* **2008**, *20*, 1456.
- [74] J. Huang, Z. Xu, Y. Yang, *Adv. Funct. Mater.* **2007**, *17*, 1966.
- [75] Y. Yuan, D. Grozea, S. Han, Z. H. Lu, *Appl. Phys. Lett.* **2004**, *85*, 4959.
- [76] Y. Li, D. Q. Zhang, L. Duan, R. Zhang, L. D. Wang, Y. Qiu, *Appl. Phys. Lett.* **2007**, *90*, 39.
- [77] Q. Liu, L. Duan, Y. Li, J. Qiao, Z. Yu, D. Zhang, L. Wang, G. Dong, Y. Qiu, *Jpn. J. Appl. Phys.* **2009**, *48*, 1023021.
- [78] J. Lee, H. Lee, P. Jeon, K. Jeong, T. Gun Kim, J. Won Kim, Y. Yi, *Appl. Phys. Lett.* **2012**, *100*, 1.
- [79] K. D. Moulder, J. F.; Stickle, W. F; Sobol, P. E.; Bomben, *Handbook of X-Ray Photoemission Spectroscopy*; Perkin-Elmer Corporation: Minnesota, 1992.
- [80] M. Lehnhardt, S. Hamwi, M. Hopping, J. Reinker, T. Riedl, W. Kowalsky, *Appl. Phys. Lett.* **2010**, *96*, 1.
- [81] P. Pingel, R. Schwarzl, D. Neher, *Appl. Phys. Lett.* **2012**, *100*.
- [82] K. K. Sze, S. M.; Ng, *Physics of Semiconductor Devices*; 3rd editio.; John Wiley and Sons: New Jersey, 2007.
- [83] M. A. Baldo, D. F. O 'brien, Y. You, A. Shoustikov, S. Sibley, M. E. Thompson, S. R. Forrest, *Nature* **1998**, *395*, 151.

- [84] C. Adachi, M. A. Baldo, M. E. Thompson, S. R. Forrest, *J. Appl. Phys.* **2001**, *90*, 5048.
- [85] H. Uoyama, K. Goushi, K. Shizu, H. Nomura, C. Adachi, *Nature* **2012**, *492*, 234.
- [86] C. W. Lee, J. Y. Lee, *Adv. Mater.* **2013**, *25*, 5450.
- [87] Y.-H. Huang, W.-L. Tsai, W.-K. Lee, M. Jiao, C.-Y. Lu, C.-Y. Lin, C.-Y. Chen, C.-C. Wu, *Adv. Mater.* **2015**, *27*, 929.
- [88] D. R. Lee, B. S. Kim, C. W. Lee, Y. Im, K. S. Yook, S. H. Hwang, J. Y. Lee, *ACS Appl. Mater. Interfaces* **2015**, *7*, 9625.
- [89] H. Kaji, H. Suzuki, T. Fukushima, K. Shizu, K. Suzuki, S. Kubo, T. Komino, H. Oiwa, F. Suzuki, A. Wakamiya, Y. Murata, C. Adachi, *Nat. Commun.* **2015**, *6*, 8476.
- [90] T.-A. Lin, T. Chatterjee, W.-L. Tsai, W.-K. Lee, M.-J. Wu, M. Jiao, K.-C. Pan, C.-L. Yi, C.-L. Chung, K.-T. Wong, C.-C. Wu, *Adv. Mater.* **2016**, *28*, 6976.
- [91] C. Y. Kuei, W. L. Tsai, B. Tong, M. Jiao, W. K. Lee, Y. Chi, C. C. Wu, S. H. Liu, G. H. Lee, P. T. Chou, *Adv. Mater.* **2016**, *28*, 2795.
- [92] K. Udagawa, H. Sasabe, F. Igarashi, J. Kido, *Adv. Opt. Mater.* **2016**, *4*, 86.
- [93] T. Komino, Y. Sagara, H. Tanaka, Y. Oki, N. Nakamura, H. Fujimoto, C. Adachi, *Appl. Phys. Lett.* **2016**, *108*, 241106.
- [94] T.-H. Han, M.-R. Choi, C.-W. Jeon, Y.-H. Kim, S.-K. Kwon, T.-W. Lee, *Sci. Adv.* **2016**, *2*, e1601428.

- [95] S. Y. Kim, W. I. Jeong, C. Mayr, Y. S. Park, K. H. Kim, J. H. Lee, C. K. Moon, W. Brutting, J. J. Kim, *Adv. Funct. Mater.* **2013**, *23*, 3896.
- [96] K.-H. Kim, S. Lee, C.-K. Moon, S.-Y. Kim, Y.-S. Park, J.-H. Lee, J. Woo Lee, J. Huh, Y. You, J.-J. Kim, *Nat. Commun.* **2014**, *5*, 4769.
- [97] J. W. Sun, J. H. Lee, C. K. Moon, K. H. Kim, H. Shin, J. J. Kim, *Adv. Mater.* **2014**, *26*, 5684.
- [98] H. Shin, J. Lee, C. Moon, J. Huh, B. Sim, J. Kim, *Adv. Mater.* **2016**, *28*, 4920.
- [99] H. Aziz, *Science (80-.)*. **1999**, *283*, 1900.
- [100] R. C. Kwong, M. R. Nugent, L. Michalski, T. Ngo, K. Rajan, Y. J. Tung, M. S. Weaver, T. X. Zhou, M. Hack, M. E. Thompson, S. R. Forrest, J. J. Brown, *Appl. Phys. Lett.* **2002**, *81*, 162.
- [101] R. Meerheim, K. Walzer, M. Pfeiffer, K. Leo, *Appl. Phys. Lett.* **2006**, *89*, 61111.
- [102] S. Scholz, K. Walzer, K. Leo, *Adv. Funct. Mater.* **2008**, *18*, 2541.
- [103] D. Y. Kondakov, R. H. Young, *J. Applid Phys.* **2010**, *108*, 74513.
- [104] Y. Zhang, J. Lee, S. R. Forrest, *Nat. Commun.* **2014**, *5*, 5008.
- [105] Q. Wang, H. Aziz, *ACS Appl. Mater. Interfaces* **2013**, *5*, 8733.
- [106] Q. Wang, H. Aziz, *Adv. Opt. Mater.* **2015**, *3*, 967.
- [107] Y. Zhang, H. Aziz, *ACS Appl. Mater. Interfaces* **2016**, *8*, 14088.
- [108] S. K. Jeon, J. Y. Lee, *Org. Electron. physics, Mater. Appl.* **2015**, *27*, 202.
- [109] Z. Wu, N. Sun, L. Zhu, H. Sun, J. Wang, D. Yang, X. Qiao, J. Chen, S.

- M. Alshehri, T. Ahamad, D. Ma, *ACS Appl. Mater. Interfaces* **2016**, *8*, 3150.
- [110] T.-H. Han, W. Song, T.-W. Lee, *ACS Appl. Mater. Interfaces* **2015**, *7*, 3117.
- [111] S. Hong, J. W. Kim, S. Lee, *Appl. Phys. Lett.* **2015**, *107*, 41117.
- [112] D. P.-K. Tsang, T. Matsushima, C. Adachi, *Sci. Rep.* **2016**, *6*, 22463.
- [113] Y. Sun, L. Duan, D. Zhang, J. Qiao, G. Dong, L. Wang, Y. Qiu, *Adv. Funct. Mater.* **2011**, *21*, 1881.
- [114] W. Y. Hung, P. Y. Chiang, S. W. Lin, W. C. Tang, Y. T. Chen, S. H. Liu, P. T. Chou, Y. T. Hung, K. T. Wong, *ACS Appl. Mater. Interfaces* **2016**, *8*, 4811.
- [115] H. Uoyama, K. Goushi, K. Shizu, H. Nomura, C. Adachi, *Nature* **2012**, *492*, 234.
- [116] *Jaguar*; version 9.; Schrodinger: New York, NY, 2016.
- [117] A. D. Bochevarov, E. Harder, T. F. Hughes, J. R. Greenwood, D. A. Braden, D. M. Philipp, D. Rinaldo, M. D. Halls, J. Zhang, R. A. Friesner, *Int. J. Quantum Chem.* **2013**, *113*, 2110.
- [118] *Materials Science Suite*; Version 2.; Schrödinger: New York, NY, 2016.
- [119] N. D. Nguyen, M. Schmeits, *Phys. Status Solidi A* **2006**, *203*, 1901.
- [120] S. Ishihara, H. Hase, T. Okachi, H. Naito, *Phys. Status Solidi C* **2012**, *9*, 2561.
- [121] S. Sato, M. Takata, M. Takada, H. Naito, *J. Nanosci. Nanotechnol.*

2016, 16, 3368.

- [122] K. K. Tsung, S. K. So, *J. Appl. Phys.* **2009**, 106, 83710.
- [123] J. M. Kim, S. J. Yoo, C. K. Moon, B. Sim, J. H. Lee, H. Lim, J. W. Kim, J. J. Kim, *J. Phys. Chem. C* **2016**, 120, 9475.
- [124] K. Takagi, T. Nagase, T. Kobayashi, H. Naito, *Appl. Phys. Lett.* **2016**, 108, 53305.
- [125] P. E. Burrows, V. Bulovic, S. R. Forrest, L. S. Sapochak, D. M. McCarty, M. E. Thompson, *Appl. Phys. Lett.* **1994**, 65, 2922.
- [126] H. Aziz, *Science (80-.)*. **1999**, 283, 1900.
- [127] W. Song, J. Y. Lee, *Adv. Opt. Mater.* **2017**.
- [128] S. Scholz, C. Corten, K. Walzer, D. Kuckling, K. Leo, *Org. Electron.* **2007**, 8, 709.
- [129] V. Sivasubramaniam, F. Brodkorb, S. Hanning, H. P. Loebel, V. Elsbergen, H. Boerner, U. Scherf, M. Kreyenschmidt, *Cent. Eur. J. Chem.* **2009**, 7, 836.
- [130] S. Scholz, R. Meerheim, B. Lüssem, K. Leo, *Appl. Phys. Lett.* **2009**, 94, 43314.
- [131] I. R. de Moraes, S. Scholz, B. Lüssem, K. Leo, *Appl. Phys. Lett.* **2011**, 99, 53302.
- [132] J. Lee, C. Jeong, T. Batagoda, C. Coburn, M. E. Thompson, S. R. Forrest, *Nat. Commun.* **2017**, 8, 15566.
- [133] L. S. Cui, S. Bin Ruan, F. Bencheikh, R. Nagata, L. Zhang, K. Inada, H. Nakanotani, L. S. Liao, C. Adachi, *Nat. Commun.* **2017**, 8, 2250.

- [134] C. S. Oh, J. M. Choi, J. Y. Lee, *Adv. Opt. Mater.* **2016**, *4*, 1281.
- [135] S.-G. Ihn, N. Lee, S. O. Jeon, M. Sim, H. Kang, Y. Jung, D. H. Huh, Y. M. Son, S. Y. Lee, M. Numata, H. Miyazaki, R. Gómez-Bombarelli, J. Aguilera-Iparraguirre, T. Hirzel, A. Aspuru-Guzik, S. Kim, S. Lee, *Adv. Sci.* **2017**, 1600502.
- [136] D. Zhang, M. Cai, Y. Zhang, D. Zhang, L. Duan, *Mater. Horiz.* **2016**, *3*, 145.
- [137] K. W. Hershey, J. Suddard-Bangsund, G. Qian, R. J. Holmes, *Appl. Phys. Lett.* **2017**, *111*, 113301.
- [138] J. S. Bangsund, K. W. Hershey, R. J. Holmes, *ACS Appl. Mater. Interfaces* **2018**, *10*, 5693.
- [139] S. Kim, H. J. Bae, S. Park, W. Kim, J. Kim, J. S. Kim, Y. Jung, S. Sul, S. G. Ihn, C. Noh, S. Kim, Y. You, *Nat. Commun.* **2018**, *9*, 1211.
- [140] N. C. Giebink, B. W. D'Andrade, M. S. Weaver, J. J. Brown, S. R. Forrest, *J. Appl. Phys.* **2009**, *105*, 124514.
- [141] R. Seifert, S. Scholz, B. Lüssem, K. Leo, *Appl. Phys. Lett.* **2010**, *97*, 13308.
- [142] Q. Wang, B. Sun, H. Aziz, *Adv. Funct. Mater.* **2014**, *24*, 2975.
- [143] T. Y. Chu, Y. H. Lee, O. K. Song, *Appl. Phys. Lett.* **2007**, *91*, 223509.
- [144] D. Y. Kondakov, *J. Appl. Phys.* **2008**, *104*, 84520.
- [145] G. Tian, W. Liang, Y. Chen, N. Xiang, Q. Dong, J. Huang, J. H. Su, *Dye. Pigment.* **2016**, *126*, 296.
- [146] M. Schmeits, *J. Appl. Phys.* **2007**, *101*, 84508.

- [147] M. Hoping, C. Schildknecht, H. Gargouri, T. Riedl, M. Tilgner, H. H. Johannes, W. Kowalsky, *Appl. Phys. Lett.* **2008**, *92*, 213306.
- [148] T. Okachi, T. Nagase, T. Kobayashi, H. Naito, *Thin Solid Films* **2008**, *517*, 1331.
- [149] S. Ishihara, T. Okachi, H. Naito, *Thin Solid Films* **2009**, *518*, 452.
- [150] B. Li, J. Chen, Y. Zhao, D. Yang, D. Ma, *Org. Electron.* **2011**, *12*, 974.
- [151] S. Ishihara, H. Hase, T. Okachi, H. Naito, *J. Appl. Phys.* **2011**, *110*, 36104.
- [152] M. Takata, N. Kouda, S. Ishihara, T. Nagase, T. Kobayashi, H. Naito, *Jpn. J. Appl. Phys.* **2014**, *53*, 02BE02.
- [153] S. Ishihara, H. Hase, T. Okachi, H. Naito, *Thin Solid Films* **2014**, *554*, 213.
- [154] J. M. Montero, J. Bisquert, G. Garcia-Belmonte, H. J. Bolink, E. M. Barea, *Phys. status solidi* **2007**, *204*, 2402.
- [155] D. C. Tripathi, A. K. Tripathi, Y. N. Mohapatra, *Appl. Phys. Lett.* **2011**, *98*, 33304.
- [156] H. Shin, J. H. Lee, C. K. Moon, J. S. Huh, B. Sim, J. J. Kim, *Adv. Mater.* **2016**, *28*, 4920.
- [157] W. Song, J. Y. Lee, Y. J. Cho, H. Yu, H. Aziz, K. M. Lee, *Adv. Sci.* **2017**, 1700608.

초 록

유기반도체에 대한 연구가 시작된 후 유기발광소자, 유기태양전지, 유기박막트랜지스터 등의 다양한 유기전자소자가 구현되었다. 특히 유기발광소자는 유기반도체의 물리, 화학적 이해를 기반으로 실용적인 디스플레이로 상용화되었다. 본 연구에서는 전기적으로 도핑된 유기반도체의 전하생성과 유기발광소자의 전하거동에 대해 탐구하였다. 2장에서는 도핑된 유기반도체의 전하생성 과정을 정량적으로 분석하였다. 전기적 도핑은 유기반도체의 전기전도도를 향상시켜 유기전자소자의 효율을 향상시키고 구동 전압을 낮추는 기술이다. 하지만 무기물 반도체와는 달리 유기반도체에서는 도펀트 대비 생성된 자유 전하의 수를 의미하는 전하생성효율이 수 %로 낮은 모습이 보고되었다. 이에 따라 여러 연구를 통해 도핑된 유기반도체에서는 호스트와 도펀트 간 전하이동복합체를 형성한 후 자유 전하로 분리된다는 것이 밝혀졌다. 본 연구에서는 분광학적 분석과 전기적 분석을 통해 n -도핑된 유기반도체의 전하생성효율을 전하이동복합체 생성 효율과 분리 효율로 나누어 정량 분석하였다. 그 결과 전하이동복합체에서 자유 전하로 분리가 되는 과정이 상대적으로 비효율적인 모습을 보여 전하생성효율이 낮음을 밝혀낼 수 있었다. 3장과 4장에서는 유기발광소자의 소자 수명 특성을 각 유기물과 소자의 전기적 특성 분석을 통해 이해하였다. 3장에서

공동호스트를 사용한 소자와 단일호스트를 사용한 소자를 비교함으로써 발광층 내의 전자이동도와 정공이동도 간의 균형이 폴라론과 여기자의 분포에 영향을 미친다는 것을 밝혀냈다. 이러한 연구결과는 이동도 균형을 맞추기 위해 공동호스트를 사용하거나 양극성 호스트를 사용하더라도 전하이동도에 대한 정량적인 분석이 중요하다는 것을 의미한다. 4장에서는 유기발광소자의 소자 수명 특성에 전하수송층이 미치는 영향에 대해서 살펴보았다. 정공수송층 구조만 다른 두 유기발광소자의 소자 수명을 측정한 결과 약 7배의 차이를 보였고 이러한 특성의 원인을 분석하였다. 다양한 정적, 동적인 전기적 특성 분석을 수행한 결과 전하수송층은 발광층 내부의 전하량을 제어하고 발광층 내부에서의 전하 이동 경로를 결정하는 역할을 하는 것을 밝혀냈다. 이 두가지 효과는 발광층 내에서 전하량과 전하이동도의 균형을 제어하는데 중요한 요인으로 작용하기 때문에 소자 수명을 극대화하기 위해서는 전하수송층에 대한 설계 또한 이러한 관점에서 고려해야한다는 것을 제시하였다.

주요어: 유기반도체, 유기발광소자, 전기적 도핑, 소자 안정성, 폴라론 거동, 임피던스 분광학, 표동-확산 모델링

학번: 2012-23928

CURRICULUM VITAE

Jae-Min Kim

Department of Materials Science and Engineering

Seoul National University, Seoul, 151-744, Korea

+82-2-875-2412 (Office)

E-mail: erda815@snu.ac.kr

Education

2012.09 ~ 2018.08 **Ph.D.** in Materials Science and Engineering

Supervisor: Professor Jang-Joo Kim

Seoul National University, Seoul, Korea

2008.03 ~ 2012.08 **B.S.** in Materials Science and Engineering

Seoul National University, Seoul, Korea

Research Interests

- Electrical characterization of organic semiconductors and organic light-emitting diodes (carrier density, carrier mobility, impedance analysis)
- Electrical doping in organic semiconductors
- Operational stability of organic light-emitting diodes

Professional Skills

- Design and fabrication of organic electronic devices: Thermal evaporator, Glove-box,

- The optoelectronic analyses on organic semiconductors: UV-vis-NIR absorption spectroscopy, Mott-Schottky analysis, analysis of impedance response of organic semiconductors, Transient photoluminescence (PL), PL efficiency measurement, angle-dependent PL analysis
- The electrical characterization of OLEDs: impedance analysis of single-carrier devices and OLEDs, drift-diffusion numerical modeling
- The photoemission spectroscopy on organic semiconductors: Ultraviolet photoelectron spectroscopy (UPS), X-ray photoelectron spectroscopy (XPS)
- Density functional theory (DFT) calculation

Scholarship and Fellowship

- Brain Korea 21 Scholarship (2012.09~)
- World Class University (WCU) project through National Research Foundation of Korea funded by the Ministry of Education, Science, and Technology (2012.09~)

List of Publications

1. **Jae-Min Kim** and Jang-Joo Kim*, "Charge Transport Layers Manage Mobility and Carrier Density Balance in Light-emitting Layers influencing the Operational Stability of Organic Light Emitting Diodes", *ACS Applied Materials & Interfaces*, submitted.
2. **Jae-Min Kim**, Chang-Heon Lee, Jang-Joo Kim*, "Mobility balance in the light-emitting layer governs the polaron accumulation and operational stability of organic light-emitting diodes", *Applied Physics Letters*, 111 (20), 203301 (2017)
3. **Jae-Min Kim**, Seung-Jun Yoo, Chang-Ki Moon, Bomi Sim, Jae-Hyun Lee*, Heeseon Lim, Jeong Won Kim, Jang-Joo Kim*, "N-type Molecular Doping in Organic Semiconductors: Formation and Dissociation Efficiencies of Charge Transfer Complex", *The Journal of Physical Chemistry C*, 120 (17), 9475-9481 (2016)
4. Seung-Jun Yoo, Jeong-Hwan Lee, **Jae-Min Kim**, Jang-Joo Kim*, "Hole mobility in various transition-metal-oxides doped organic semiconductor films", *Applied Physics Letters*, 110 (5), 053303 (2017)
5. Jeong-Hwan Lee, Hyun Shin, **Jae-Min Kim**, Kwon-Hyeon Kim, Jang-Joo Kim*, "Exciplex-Forming Co-Host-Based Red Phosphorescent Organic Light-Emitting Diodes with Long Operational Stability and High Efficiency", *ACS Applied Materials & Interfaces*, 9 (4), 3277-3281 (2017)

List of Presentations

International Conference

1. **Jae-Min Kim**, Chang-Heon Lee, Jang-Joo Kim, "Accumulated Polaron in Light-Emitting Layer Governs the Operational Stability of Organic Light-Emitting Diodes", The 17th International Meeting on Information Display (iMiD 2017), August 28-31 (August 31), 2017, Korea
2. **Jae-Min Kim**, Seung-Jun Yoo, Chang-Ki Moon, Bomi Sim, Jae-Hyun Lee, Heeseon Lim, Jeong Won Kim, Jang-Joo Kim, "N-type Electrical Doping in Organic Semiconductors: Formation and Dissociation Efficiencies of Charge Transfer Complex", International Conference on Electronic Materials and Nanotechnology for Green Environment (ENGE 2016), November 6-9 (November 07), 2016, Korea
3. **Jae-Min Kim**, Seung-Jun Yoo, Chang-Ki Moon, Bomi Sim, Jae-Hyun Lee, Heeseon Lim, Jeong Won Kim, Jang-Joo Kim, "n-type molecular electrical doping in organic semiconductors: formation and dissociation efficiencies of charge transfer complex", SPIE Optics+Photonics 2016, August 28-September 1 (August 29), 2016, USA
4. **Jae-Min Kim**, Seung-Jun Yoo, Jeong-Hwan Lee, Chang-Ki Moon, Bomi Sim, Jae-Hyun Lee, Heeseon Lim, Jeong Won Kim, Jang-Joo Kim, "n-type molecular doping in organic semiconductors: Formation and dissociation efficiencies of charge transfer complex", The International Symposium on

Recent Advances and Future Issues in Organic Electroluminescence

(ISOEL2016), February 17-19 (February 18), 2016, Korea

5. **Jae-Min Kim**, Seung-Jun Yoo, Chang-Ki Moon, Bomi Sim, Heeseon Lim, Jeong Won Kim, Jae-Hyun Lee, Jang-Joo Kim, "N-type molecular doping in organic semiconductors: Formation and dissociation efficiencies of charge transfer complex", The 7th International Workshop on Flexible & Printable Electronics 2015 (IWFPE 2015), November 4-6 (November 5), 2015, Korea
6. Hyun Shin, Jeong-Hwan Lee, **Jae-Min Kim**, Kwon-Hyeon Kim, Jang-Joo Kim, "Stable Red Phosphorescent Organic Light-emitting Diodes using exciplex forming co-host with High Efficiency", The 9th Asian Conference on Organic Electronics (A-COE 2017), October 25-27 (October 26), 2017, Korea
7. Chang-Ki Moon, Jin-Suk Huh, **Jae-Min Kim**, Jang-Joo Kim, "Electronic Structures and Emission Processes of Exciplex depending on Dimer Geometries in Solid States", The 17th International Meeting on Information Display (iMiD 2017), August 28-31 (August 31), 2017, Korea
8. Chang-Ki Moon, Jin-Suk Huh, **Jae-Min Kim**, Jang-Joo Kim, "Electronic structures and emission processes of exciplex depending on dimer configurations", 2nd International TADF Workshop, July 19-21 (July 19), 2017, Japan
9. Seung-Jun Yoo, Jeong-Hwan Lee, **Jae-Min Kim**, Jang-Joo Kim, "Hole mobility in various p-doped organic semiconductor films", 25th Anniversary KVS Symposium (25th KVS), August 21-26 (August 25), 2016, Korea

10. Seung-Jun Yoo, Jeong-Hwan Lee, **Jae-Min Kim**, Jang-Joo Kim, "Effect of negatively ionized p-dopants on hole mobility in various organic hosts with different energetic disorder parameters", The International Symposium on Recent Advances and Future Issues in Organic Electroluminescence (ISOEL2016), February 17-19 (February 18), 2016, Korea
11. Seung-Jun Yoo, Jeong-Hwan Lee, **Jae-Min Kim**, Jang-Joo Kim, "Correlation of charge mobility with energetic disorder of host molecules in p-doped organic semiconductors", 2015 International Chemical Congress of Pacific Basin Societies (Pacifichem 2015), December 15-20 (December 17), 2015, USA
12. Seung-Jun Yoo, Jeong-Hwan Lee, **Jae-Min Kim**, Jang-Joo Kim, "Effect of electrical doping on hole mobility and energetic disorder in p-doped amorphous organic semiconductors", The 7th International Workshop on Flexible & Printable Electronics 2015 (IWFPE 2015), November 4-6 (November 5), 2015, Korea
13. Seung-Jun Yoo, Jeong-Hwan Lee, **Jae-Min Kim**, and Jang-Joo Kim, "Correlation of Charge Mobility with Energetic Disorder of Host Molecules in p-doped Disordered Organic Semiconductors", KJF-ICOMEF 2015, September 6-9 (September 8), 2015, Korea
14. Seung-Jun Yoo, Jeong-Hwan Lee, **Jae-Min Kim**, Jang-Joo Kim, "Correlation of carrier mobility with energetic disorder of host molecules in p-doped amorphous organic semiconductors", SPIE Optics+Photonics 2015, August 9-13 (August 10), 2015, USA

Domestic Conference

1. 김재민, 유승준, 문창기, 심봄이, 이재현, 임희선, 김정원, 김장주, "n-Type electrical doping in organic semiconductors: Formation and dissociation efficiencies of charge transfer complex", 2016 한국고분자학회 춘계학술대회, April 6-8 (April 7), 2016, Korea
2. 신현, 이정환, 김재민, 김권현, 김장주, "Red Phosphorescent Organic Light-emitting Diodes Using Exciplex Forming Co-host with Long Operational Lifetime and High Efficiency", 2017 한국고분자학회 추계학술대회, October 11-13 (October 12), 2017, Korea
3. 유승준, 이정환, 김재민, 김장주, "Correlation of charge mobility with energetic disorder of host molecules in p-doped disordered organic semiconductors", 2015 한국고분자학회 춘계학술대회, April 8-10 (April 9), 2015, Korea

List of Patents

김장주, 김재민, "공동 호스트를 포함하는 유기 발광 소자", 출원번호 10-2017-0067632 (2017.05.31)